J Nanotechnol Res 2022; 4 (2): 059-096 *DOI: 10.26502/ jnr.2688-85210031*

Research Article

Hypergolic Materials Synthesis: A Review

Athanasios B Bourlinos[1,*], Nikolaos Chalmpes[2], Dimitrios Gournis[2], Michael A. Karakassides[2]

[1]Physics Department, University of Ioannina, 45110 Ioannina, Greece

[2]Department of Materials Science & Engineering, University of Ioannina, 45110 Ioannina, Greece

[*]**Corresponding Author:** Athanasios B. Bourlinos, Physics Department, University of Ioannina, 45110 Ioannina, Greece. Tel: +302651008511.

Received: 23 March 2022; **Accepted:** 07 April 2022; **Published:** 30 April 2022

Citation: Athanasios B Bourlinos, Nikolaos Chalmpes, Dimitrios Gournis, Michael A Karakassides. Hypergolic Materials Synthesis: A Review. Journal of Nanotechnology Research 4 (2022): 59-96.

Abstract

Hypergolic materials synthesis is a new preparative technique in materials science that allows a wide range of carbon (nanosheets, dots, hollow spheres, discs, fullerols, graphene/graphite) or inorganic (magnetic, photocatalytic, metallic or metal alloy) solids with useful properties to be obtained. Solely based on simple hypergolic reactions that lift-off rockets to space, the method not only allows the fast and spontaneous synthesis of several nanomaterials at ambient conditions, but also releases sizable amounts of energy that can be directly converted into useful work, such as chemical, mechanical, photovoltaic, thermoelectric or heating fluids. The present review aims to summarize the basic principles behind this new technique, to emphasize the general character and simplicity of the method by citing several paradigms of carbon and inorganic functional materials syntheses, as well as, to discuss some future prospects for large scale implementation based on rocket fuel engineering concepts.

Keywords: Carbon materials; Hypergolic materials synthesis; Hypergolic reactions; Inorganic materials; Rocket fuel engineering

1. Introduction

Progress in materials science largely depends on new synthesis methods and techniques. So far these include solid-state, ball-milling, arc-discharge, plasma, pyrolytic, template synthesis, nanolithography, High Pressure-High Temperature (HPHT), sol-gel, sol-gel autocombustion, freeze-drying, micro emulsion, precipitation, borohydride reduction, thermolysis, hot-injection, sonochemical, hydrothermal, chemical vapor deposition, sputtering, flame spray pyrolysis, electrochemical and microwave synthesis [1-4]. In spite of the large variety of existing techniques today, there is an ever-increasing demand for new synthesis

methods in materials science that could deal with needs not met by the previous ones. Hypergolic materials synthesis has been recently introduced from our group as a radically new preparative technique in materials science [5-14]. Based on simple hypergolic reactions used to lift-off rockets in space, the new technique displays certain advantages as following: (i) it is simple and easy in operation; (ii) it is of general character towards both carbon and inorganic materials syntheses; (iii) the targeted materials are formed rapidly and spontaneously at ambient conditions; (iv) it releases significant energy that can be directly converted into useful work (chemical, mechanical, photovoltaic, thermoelectric or heating fluids), *i.e.*, hypergolic materials synthesis is an energy-liberating process that clearly differentiates preparative techniques requiring energy to perform synthesis (*e.g.*, energy-consuming processes); and (v) it provides a practical way of converting disposed rocket fuel (also known as "mélange") into useful material. On the other hand, the cost and toxicity of the reagents used in hypergolic materials synthesis along with safety issues associated with hypergolic ignition are parameters that should be critically taken into consideration in view of real investment and sustainability. In this review we first give some basic definitions of hypergolic reactions, the latter being at the heart of hypergolic materials synthesis. Following, we provide several paradigms pertaining to the synthesis of carbon and inorganic functional materials using a variety of chemical precursors and oxidizers combined. Particular emphasis is given on the synthesis, characterization and practical applications of the derived materials, as well as, on the direct exploitation of the released hypergolic energy in produce useful work at spot. Lastly, we discuss the possibility towards the large scale implementation of hypergolic materials synthesis in pilot reactors that pretty much resemble the setup of chemical rocket engines. With the pros and cons, hypergolic materials synthesis definitely merits further basic and technical studies before a widespread use in labs or industry. As such, the present review provides a descriptive account of the method aiming to stimulate further research and development in this context.

2. Hypergolic reactions

Hypergolic reactions are essential in lifting off rockets to space as the means through which hypergolic fuels or propellants work [15]. Conceptually, in this type of reactions a fuel and a strong oxidizer ignite spontaneously upon contact at ambient conditions without external stimuli (Figure 1). Unlike an explosion event, where energy is released in a violent manner, in hypergolic ignition the energy is released in a smooth and continuous manner, provided that the involved reagents are slowly mixed together.

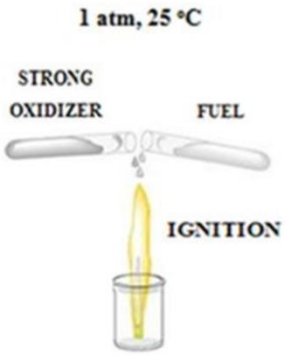

Figure 1: Schematic representation of hypergolic reactions. This type of reactions is fast and spontaneous at ambient conditions.

A typical example refers to the aniline-fuming nitric acid HNO_3 hypergolic pair shown in Figure 2, which was used in 40's to launch rocket WAC Corporal. Aniline and fuming nitric acid HNO_3 react exothermically upon contact at ambient conditions as following:

$$5\ C_6H_5NH_2 + 31\ HNO_3 \rightarrow 30\ CO_2 + 18\ N_2 + 33\ H_2O$$

Where HNO_3 serves as the source of O_2 for the exothermic combustion of aniline ($\Delta H < 0$). Likewise the exothermic decomposition of explosives, the formation of N_2 with a strong triple bond (940 kJ mol^{-1}) favors the exothermic character of the reaction. At the same time, the release of gases secures a positive entropy change as moving from the liquid reactants to the gaseous products ($\Delta S > 0$). Based on the thermodynamic definition of a reaction's free energy change ($\Delta G = \Delta H - T\Delta S$) and the algebraic signs of ΔH and ΔS, we conclude $\Delta G < 0$, *i.e.*, hypergolic reactions are thermodynamically spontaneous at ambient conditions. On the other hand, the reaction proceeds instantaneously as a result of zero spin change upon moving from reactants to products (*e.g.*, reactants and products in the above equation are all diamagnetic species having zero spin). Such reactions are spin allowed and therefore associated with a small activation energy E_a and fast kinetics. What's more, the high concentration of the reactants may also contribute to a fast reaction rate. Besides the aniline-fuming nitric acid HNO_3 hypergolic pair presented above, many more fuel-oxidizer hypergolic compositions incorporating a wide range of fuel compounds and strong oxidizers also exist, thus potentially providing an arsenal of chemical options for materials synthesis. Nevertheless, the use of hypergolic pairs and reactions as valuable synthetic tools in materials science has been only recently recognized from our group. In this frame, below we provide a concise summary of the carbon and inorganic materials that can be obtained through hypergolic materials synthesis using various hypergolic combinations of chemical precursors and oxidizers.

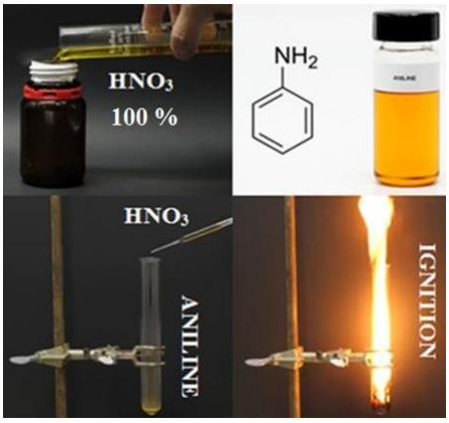

Figure 2: Dropwise addition of fuming nitric acid HNO_3 to aniline instantly triggers ignition of the hypergolic mixture inside the "rocket" test tube.

3. Hypergolic synthesis of carbon materials

Taking into consideration the central role of carbon in materials science and synthesis, hypergolic reactions can certainly provide an energy-saving and thermodynamically favored alternative towards the direct synthesis of carbon materials at ambient conditions starting from organic compounds as fuel. In this respect, no external source of heat is required to carbonize the organic compound, such as energy-consuming ovens operating at elevated temperature. As a matter of fact, hypergolic reactions release sizeable amounts of energy that can be further exploited in the production of useful work (mechanical,

electrical, chemical *etc.*) [5-13]. In addition, such reactions are kinetically favored, thus allowing rapid product formation at room temperature and atmospheric pressure (*e.g.*, within few seconds). The main purpose of this section is to highlight the importance of hypergolic reactions in the area of carbon materials synthesis. To this aim, we provide examples of hypergolic reactions that directly lead to the formation of different types of functional carbon materials at ambient conditions. Functional carbon materials include carbon nanosheets, nanodiscs, photoluminescent carbon dots, hollow spheres, graphene/graphite and fullerols. In the following, hypergolic syntheses are categorized by the type of strong oxidizer in use: fuming nitric acid HNO_3, sodium peroxide Na_2O_2, chlorine Cl_2, bromine Br_2 and self-ignition.

3.1. Fuming nitric acid HNO_3

Fuming nitric acid HNO_3 is a powerful oxidizer commonly used in hypergolic compositions. A total of five examples are discussed in this section as follows: nitrile gloves, Girard's reagent T, 1,3-cyclodienes, conductive polymers and furfuryl alcohol. In the first example, the hypergolic ignition of disposable nitrile gloves (acrylonitrile butadiene rubber) by fuming nitric acid HNO_3 resulted in the formation of carbon nanosheets [7], thus offering a practical way to transform this waste plastic into a valuable carbon product (Figure 3).

Figure 3: Fuming nitric acid HNO_3 caused ignition of nitrile glove inside a glass test tube, leading to the formation of carbon foam (far-right photo). Crashing and purification of the foam gave a fine carbon powder (far-right inset).

TEM examination of the as-derived carbon confirmed the presence of micron-sized nanosheets with smooth surface and exhibiting a multilayer texture near the edges due to the phylomorphous structure of the carbon solid (Figure 4, top). From the height profiles of the AFM inspection, the average thickness of the nanosheets was estimated between 2 and 2.5 nm (Figure 4, bottom).

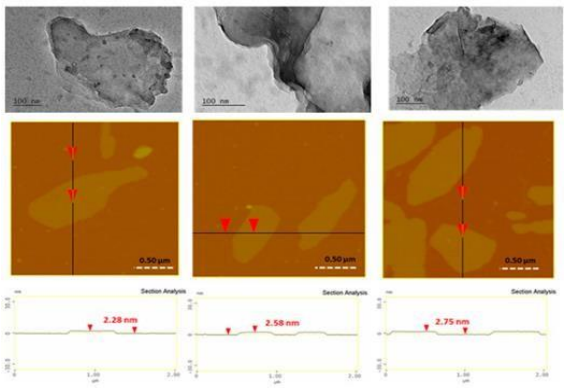

Figure 4: Representative TEM images of the sheets (top); AFM images of cross-sectional analysis of selected carbon nanosheets (bottom).

A practical application of the as-derived carbon nanosheets referred to Cr(VI) removal from wastewaters. Hexavalent chromium Cr(VI) is used in several industrial processes that produce acidic wastewaters with high levels of this toxic and carcinogenic species [16]. Hence, the removal of Cr(VI) from industrial wastewaters before releasing them into the environment becomes a great necessity. Figure 5 shows the effectiveness of the carbon nanosheets in Cr(VI) removal at initial concentration of 6 mg/L as a function of time for pH 3 at 25 °C. Accordingly, the chromium removal efficiency after 24 h reached 50 % under acidic conditions. Such a removal efficiency is of particular importance taking into consideration that the maximum allowed concentration of Cr(VI) in natural waters is 0.1 mg/L while that of drinking water 0.05 mg/L (*i.e.*, half amount 50 %).

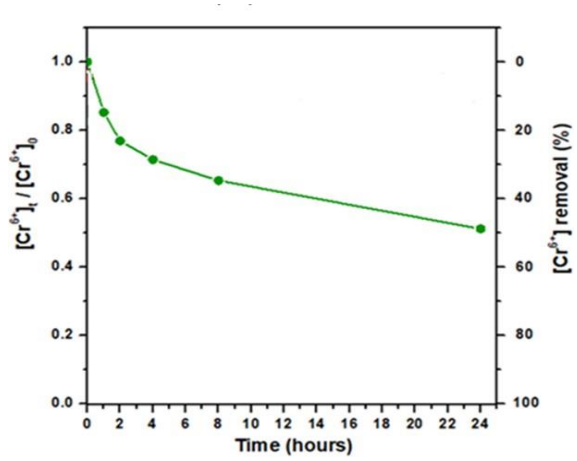

Figure 5: Effect of time on Cr(VI) removal by the carbon nanosheets for pH 3 at 25 ^{o}C.

The heat produced from the reaction of nitrile glove with fuming nitric acid HNO_3 was exploited for the rapid thermal transformation of a suitable molecular precursor into graphitic carbon nitride. To this aim, the middle finger glove tip from a medium size nitrile glove was cut out and stuffed with dichloroisocyanuric acid, sodium salt hydrate (sodium troclosene or pool chlorine). In general, triazines are considered well-suited precursors towards the formation of graphitic carbon nitride by heat [17]. The stuffed tip was hermitically folded and placed at the bottom of an alumina crucible followed by the addition of fuming nitric acid HNO_3. The ignition of the nitrile wrap provided the necessary heat for the thermal transformation of the enclosed white-colored triazine derivative into yellow graphitic carbon nitride, thus acting as a sort of a “heating stove”. After cooling, the inner product was mechanically separated from the outer carbon debris in the form of yellow chunks. The chunks were crashed into a fine powder and washed several times to afford a yellow graphitic carbon nitride powder (Figure 6).

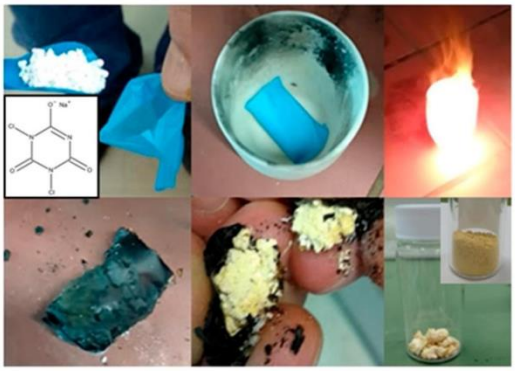

Figure 6: Top left to right bottom: the middle finger glove tip from a medium size nitrile glove was cut out and stuffed with granular dichloroisocyanuric acid, sodium salt hydrate (top inset structure). The stuffed tip was hermitically folded and placed at the bottom of an alumina crucible. After the quick addition of fuming nitric acid HNO_3, the nitrile wrap was ignited, providing the necessary heat for the thermal transformation of the enclosed triazine derivative into graphitic carbon nitride. The inner product was mechanically separated from the outer carbon debris in the form of yellow chunks (glass vial at far-right bottom). Purification of the chunks afforded yellow graphitic carbon nitride powder (bottom inset).

In the second example, the hydrazide derivative Girard's reagent T was instantly ignited upon contact with the strong oxidizer releasing brown fumes and an intense flame (Figure 7) [7]. Simultaneously, a brown residue was formed that after it had been carefully collected and dialyzed gave a clear yellowish dispersion of carbon dots in water with an average size of 5-6 nm based on AFM (Figure 8).

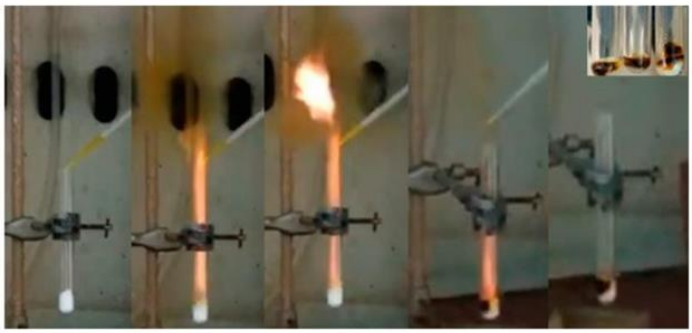

Figure 7: Dropwise addition of fuming nitric acid HNO_3 to Girard's reagent T ignited the hydrazide derivative, thus resulting in a water-soluble brown residue on the walls of the test tube (see inset).

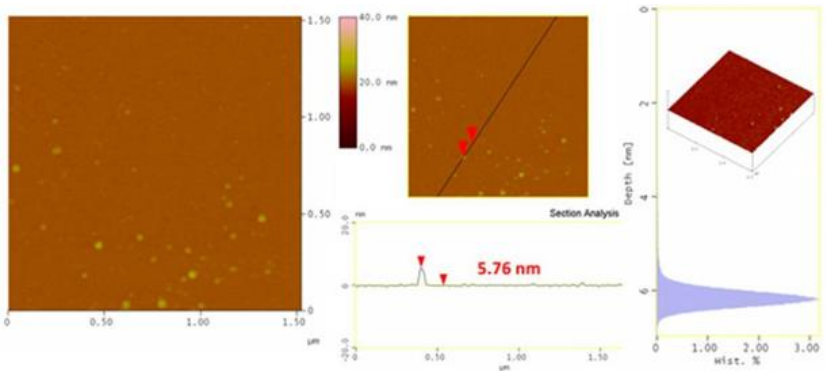

Figure 8: Topography images of the as-derived carbon dots (section-analysis, 3D morphology, and depth-analysis histograms are included).

The dispersed dots fluoresced in the visible region (Figure 9, left). With respect to the fluorescence spectra (Figure 9, right), when the excitation wavelength varied from 350 to 600 nm, the spectra red shifted and the fluorescence intensity decreased gradually. Such excitation-depended emission behavior is consistent with photoluminescent carbon dots [18-20].

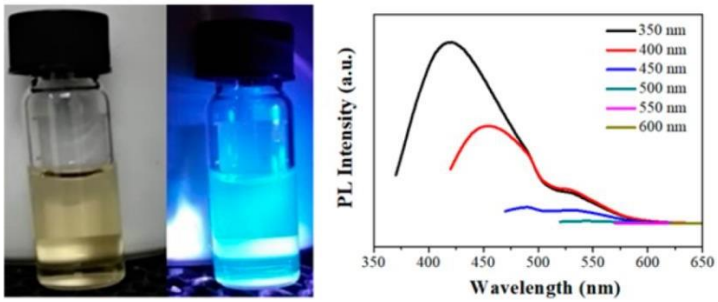

Figure 9: Aqueous dispersion of the as-prepared carbon dots under natural and UV light (left); Fluorescence emission spectra of the dots at different excitation wavelengths (λ_{ex} as inset) (right).

In the third example, 1,3-cycodienes, such as cyclopentadienyllithium, 1,3-cyclohexadiene and 1,3-cyclooctadiene, also reacted hypergolically with fuming nitric acid HNO_3 at ambient conditions to afford fine carbon powders as shown in Figure 10 [10,13] .

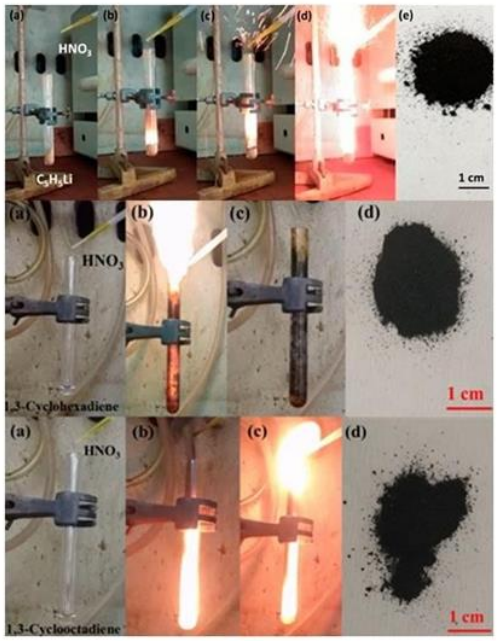

Figure 10: Hypergolic ignition of 1,3-cyclodienes by fuming nitric acid HNO_3. Top: cyclopentadienyllithium; Middle: 1,3-cyclohexadiene; Bottom: 1,3-cyclooctadiene (the labels on the photos show the gradual evolution of the phenomenon before and after addition of the strong oxidizer). The residues within the tubes were collected and washed thoroughly to afford fine

carbon powders (far-right photos).

In the case of the cyclopentadienyllithium-derived carbon a disc-like morphology was mainly observed with an average thickness of *ca.* 1 nm per nanodisc (*i.e.*, close to the thickness of graphene) (Figure 11). This type of morphology might be ascribed to the starting cyclopentadiene ring, which generally favors the formation of round-shaped nanostructures.

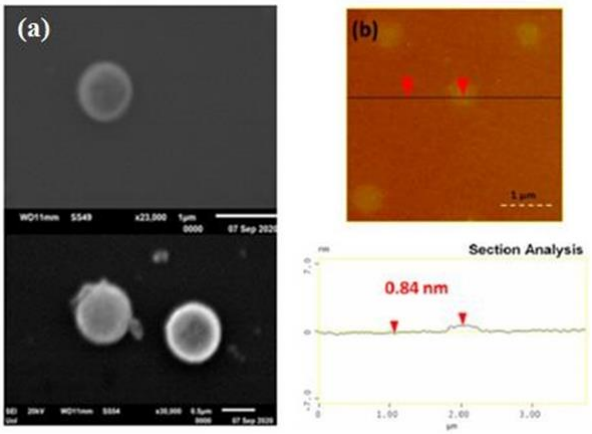

Figure 11: (a) SEM images of carbon discs; (b) AFM images of cross-sectional analysis of the carbon discs with thickness of *ca.* 1nm.

On the other hand, in the cases of 1,3-cyclohexadiene- and 1,3-cyclooctadiene-derived carbons SEM study showed the formation of carbon nanosheets displaying multilayer structure near the edges due to stacks of individual layers (Figure 12). The thickness of the nanosheets according to AFM examination was in the range 1.8-2.5 nm (Figure 13).

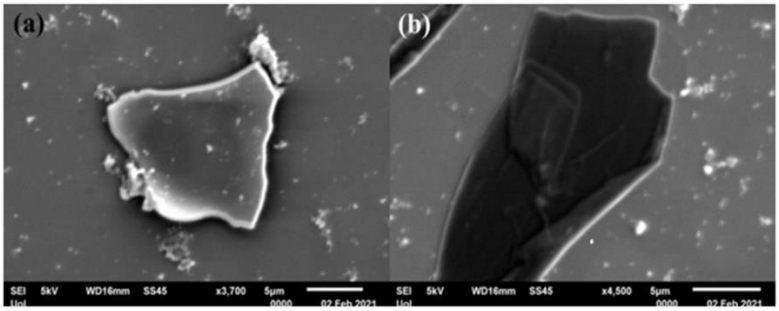

Figure 12: SEM images of (a) 1, 3-cyclohexadiene- and (b) 1, 3-cyclooctadiene-derived carbon nanosheets.

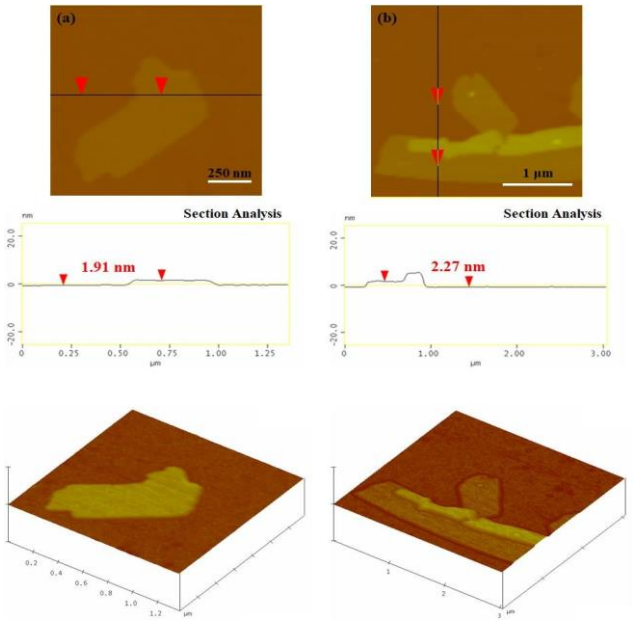

Figure 13: AFM images of cross-sectional analysis and 3D morphologies of (a) 1,3-cyclohexadiene- and (b) 1,3-cyclooctadiene-derived carbon nanosheets.

The energy released from the above-mentioned hypergolic reactions was further exploited for the production of useful chemical work. In one example, the flame produced from the ignition of 1,3-cyclohexadiene was used for the thermal decomposition of ammonium dichromate into Cr_2O_3 (the "chemical volcano" experiment), thus presenting a mini flame-pyrolysis burner set off by a hypergolic reaction (Figure 14). For this purpose, a metallic spatula loaded with ammonium dichromate was held above the top rim of the "rocket" test tube in direct contact with the released flame. Cr_2O_3 is a useful green pigment in the paint industry, as well as, an efficient catalyst toward NH_3 oxidation in the Ostwald process for making nitric acid. In another example, the flame produced from the ignition of the 1,3-cyclooctadiene-HNO_3 pair was used to heat expandable graphite (graphite bisulfate $C_{24}^{+}HSO_4^{-}$, Sigma-Aldrich) in an aluminum cup (Figure 15). Upon contact of the cup with the flame, the lustrous graphite flakes turned into foam. Such an expansion resulted from the thermal decomposition of the intercalated sulfate species into SO_2 gas, the latter pushing the graphite layers apart. The produced foam is considered an excellent absorbent material for oil removal, as well as, a suitable thermal insulator and flame retardant.

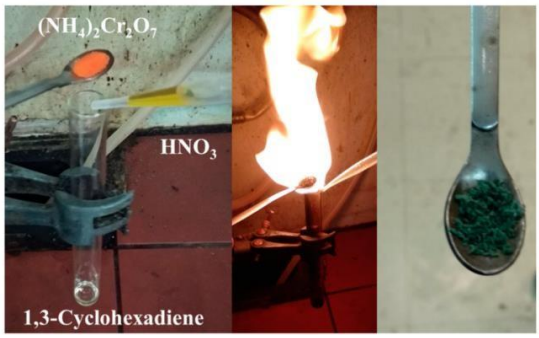

Figure 14: The flame produced from the ignition of 1,3-cyclohexadiene by fuming nitric acid HNO_3 was used for the thermal decomposition of ammonium dichromate $(NH_4)_2Cr_2O_7$ (orange solid) into Cr_2O_3 pigment and catalyst (green solid), thus presenting a mini flame pyrolysis burner set off by a hypergolic reaction.

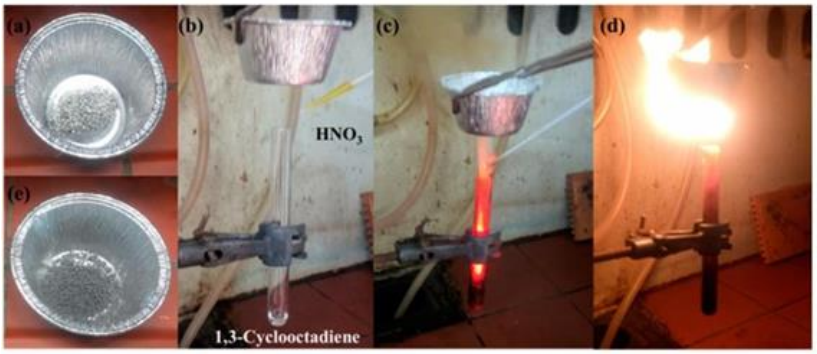

Figure 15: (a) The starting expandable graphite flakes in an aluminum cup; (b-d) The hypergolic reaction between 1,3-cyclooctadiene and fuming nitric acid HNO_3 provided the necessary heat for the thermal expansion of the flakes into foam (e).

In the fourth example of conductive polymers, the ignition of the polyaniline (or PANI)-HNO_3 hypergolic pair led to carbon nanosheets with an average thickness of 2.6 nm (Figures 16 & 17) [12].

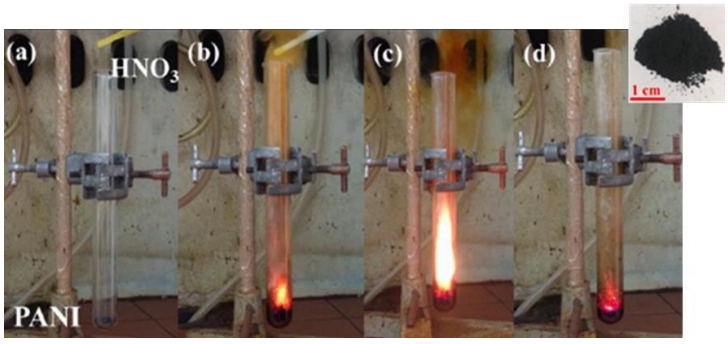

Figure 16: (a) The test tube containing polyaniline (PANI) before fuming nitric acid HNO_3 addition. (b-d) Dropwise addition of the acid sparked ignition, emitting an intense burst of flame. The residue within the tube was collected and washed extensively to afford a fine dark-brown powder (right inset).

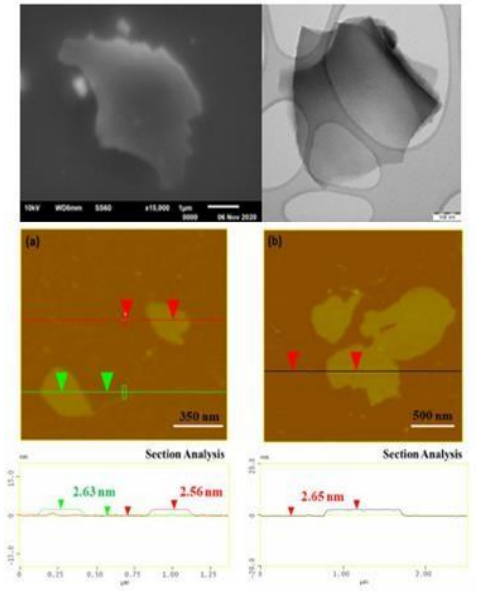

Figure 17: Top: representative SEM (left) and TEM (right) micrographs of the polyaniline-derived carbon nanosheets. Bottom: AFM images of cross-sectional analysis of selected carbon nanosheets (a,b).

It was further possible to produce single sheets from the polyaniline-derived nanosheets using the liquid-phase exfoliation technique [21]. To this aim, the carbon solid was suspended by sonication in dimethylformamide and after it had been left in rest for few days, the supernatant was collected as a clear colloid giving strong Tyndall effect using a green or red laser pointer (Figure 18b). AFM study clearly revealed the presence of single sheets in the colloid with thickness of 0.9-1.3 nm, *i.e.*, less than the average thickness of the starting nanosheets (2.6 nm) (Figures 18a,c).

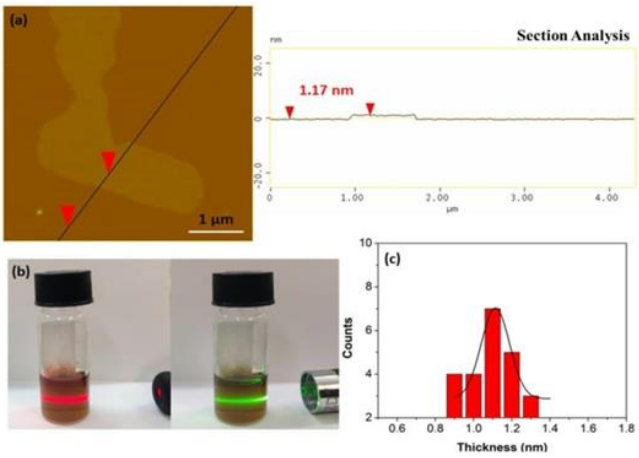

Figure 18: (a) AFM height profile of a single sheet; (b) The colloidal dispersion of the single sheets in dimethylformamide exhibiting strong Tyndall effect using a red or green laser pointer. (c) The corresponding AFM statistical analysis of thickness for the single sheets.

The method could be successfully extended to other conductive polymers, beyond polyaniline, towards the preparation of different type carbon nanostructures. For example, conductive polythiophene (PT) and polypyrrole (PPy) also reacted hypergolicly with fuming nitric acid HNO_3 to produce multi-colored emissive carbon dots (Figure 19). Based on AFM studies,

in both cases the dots appeared nearly spherical in shape with narrow size distribution of 5-7 nm (Figure 19). In addition, they were dispersible in acetone giving bright photoluminescence upon UV irradiation: the polythiophene-derived dots gave red-emission (Figure 19a), whereas those from polypyrrole green-emission [22] (Figure 19b). The different emissive properties of the dots probably reflected the different effect of heteroatom doping (S- *vs.* N-doped dots). The derived dots were further utilized to fabricate a photoluminescent polymer nanocomposite. A predetermined quantity of low polydispersity diblock copolymer polystyrene-b-polybutadiene (PS-b-PB) synthesized exclusively by anionic polymerization [23] was diluted in THF and mixed with a small amount of polythiophene-derived dots under stirring. The nanocomposite film was fabricated by casting and evaporating the solvent in a Petri dish. The completely dried film was carefully taken off from the bottom of the dish to give a photoluminescent self-standing membrane (Figure 20).

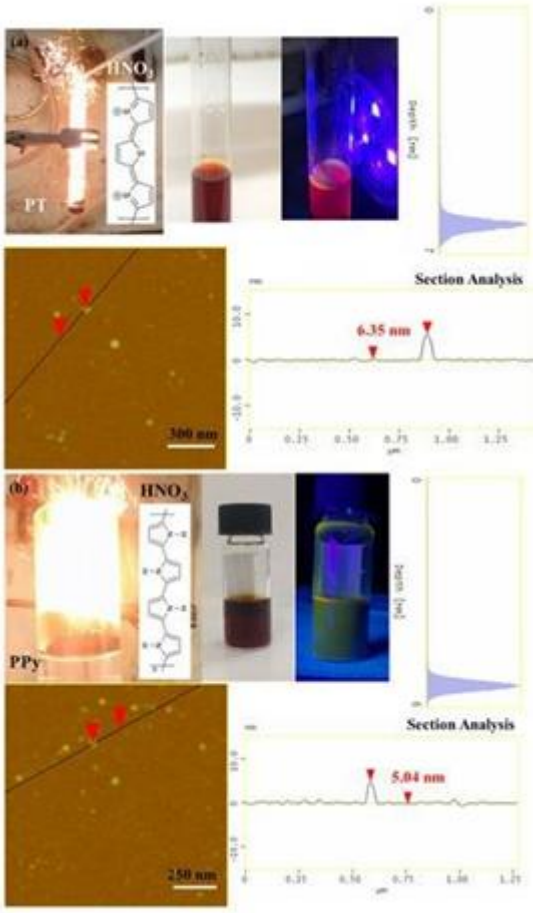

Figure 19: Hypergolic ignition of PT (a) and PPy (b) by fuming nitric acid HNO_3 resulted in photoluminescent carbon dots (see for instance the corresponding acetone dispersions under natural and UV light). The AFM topography images of (a) PT- and (b) PPy-derived dots along with their section-analysis and depth-analysis histograms are also included.

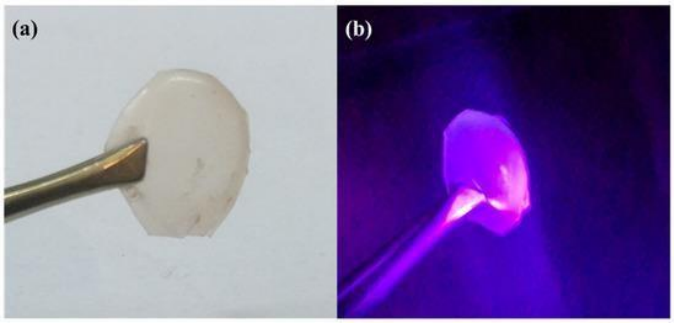

Figure 20: The red photoluminescent polymer nanocomposite containing polythiophene-derived dots under natural (a) and UV light (b).

In the last fifth example, nanocarbon was produced from rocket fuel waste based on the furfuryl alcohol-HNO_3 hypergolic pair [11]. Furfuryl alcohol is an important green chemical derived from plant raw material (corncobs, agricultural waste) through simple reaction cascades [24, 25]. A notable use of furfuryl alcohol pertains to hypergolic rocket propellants and fuels [26-29]. In this case, the renewable alcohol and fuming nitric acid HNO_3 react immediately and energetically upon contact to release heat and gases that promote rocket lift-off (WAC Corporal, Nike Ajax). Due to the vegetable origin of the organic compound, furfuryl alcohol fuel rocketry has been aptly highlighted in science blogs under imaginative headlines, such as "Flying to the Mars on Corncobs" (see for instance the link: https://dalinyebo.com/furfuryl-alcohol-rocket-fuel-then-and-now/). Hence, the furfuryl alcohol-HNO_3 pair certainly drew our attention towards the hypergolic synthesis of carbon. From a materials science viewpoint, this example also provides a practical way in dealing with rocket fuel waste or rocket fuel disposal. This is important since there is an increasing need for disposing aged stored rocket fuels (known as "mélange") in a useful manner. The hypergolic reaction of furfuryl alcohol with fuming nitric acid HNO_3 is shown in Figure 21. The carbonization of the organic precursor proceeded in two steps. In the first step, the alcohol underwent acid-catalyzed polymerization towards the formation of poly(furfuryl alcohol) [30]. In the second step, the energy released from the hypergolic pair provided the necessary heat and temperature needed for the in situ carbonization of poly(furfuryl alcohol). Indeed, the temperature during hypergolic ignition reached a maximum of nearly 300 °C within 30 s, based on the thermal camera images shown in Figure 22. This temperature matched well the decomposition point of the polymer, the latter falling in the range 200-300 °C [31,32].

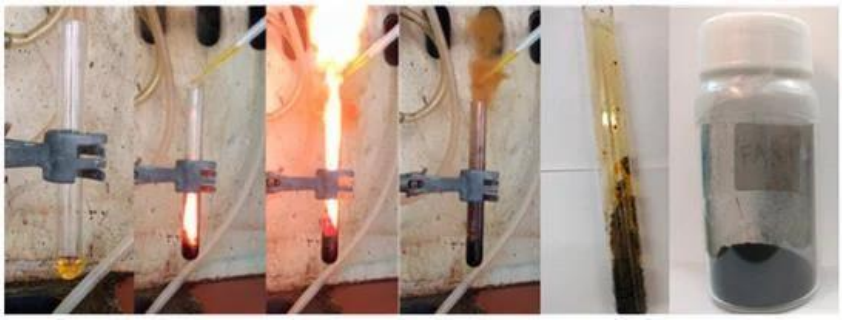

Figure 21: Fuming nitric acid HNO_3 and furfuryl alcohol reacted energetically upon contact to form a crude carbon residue inside the "rocket" test tube. Collection and washing of the residue afforded a fine carbon powder. Notice the release of brown nitrogen oxide gases as a result of HNO_3 decomposition by furfuryl alcohol.

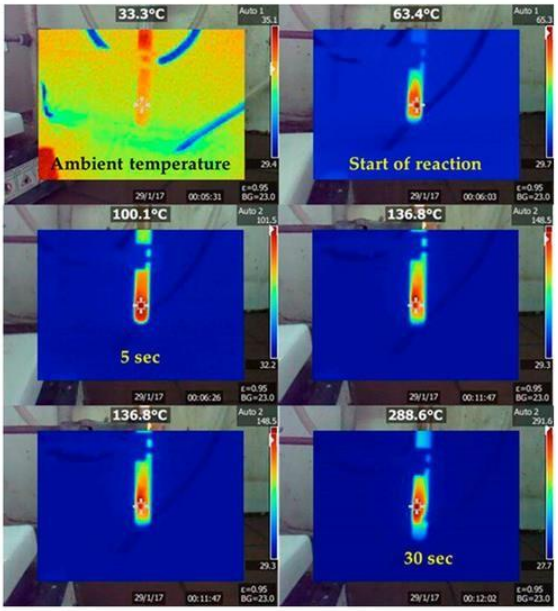

Figure 22: Temperature profile of the hypergolic reaction over time as depicted with a digital thermal camera. The temperature was raised progressively from ambient to a maximum of nearly 300 °C within 30 s.

At the same time, SEM and TEM portraits revealed exclusively the presence of nanosheets in the furfuryl alcohol-derived carbon (Figure 23, left). The nanosheets appeared compact, possessed micron-sized lateral dimensions and exhibited multi-layered texture near the edges. The average thickness of the sheets as evaluated by AFM microscopy was close to 5 nm (Figure 23, right).

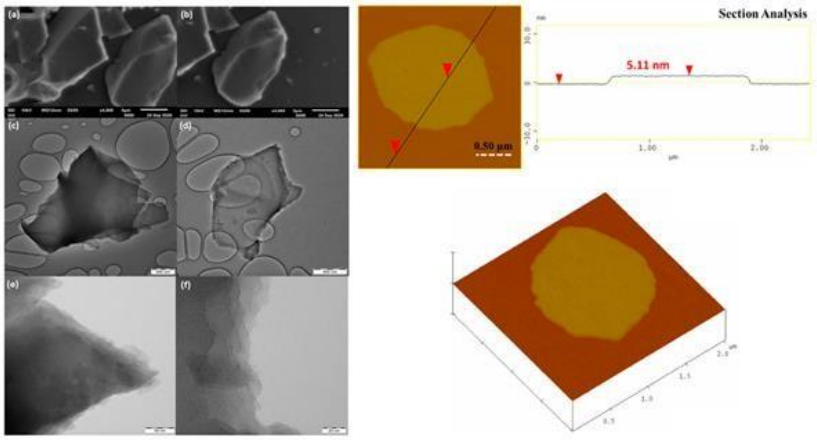

Figure 23: Left: SEM (a,b) and TEM (c-f) images of carbon nanosheets; Right: AFM images of cross-sectional analysis and 3D morphology of a selected carbon nanosheet.

The heat released from the hypergolic reaction between furfuryl alcohol and fuming nitric acid HNO_3 was exploited in various ways to produce useful work. In a first example, it was possible to boil acetone without using a heating device (Figure 24, top). This example was inspired by the popular chemistry demonstration experiment of boiling acetone through the exothermic dissolution of sulfuric acid in water. Worth noting, the operation of boiler heaters very much depends on similar energy transfer from an exothermic reaction, such as oil combustion, to a fluid, such as water. In a second example, the

reaction heat was directly converted into mechanical motion through a heat engine (*e.g.*, Crookes radiometer) (Figure 24, bottom).

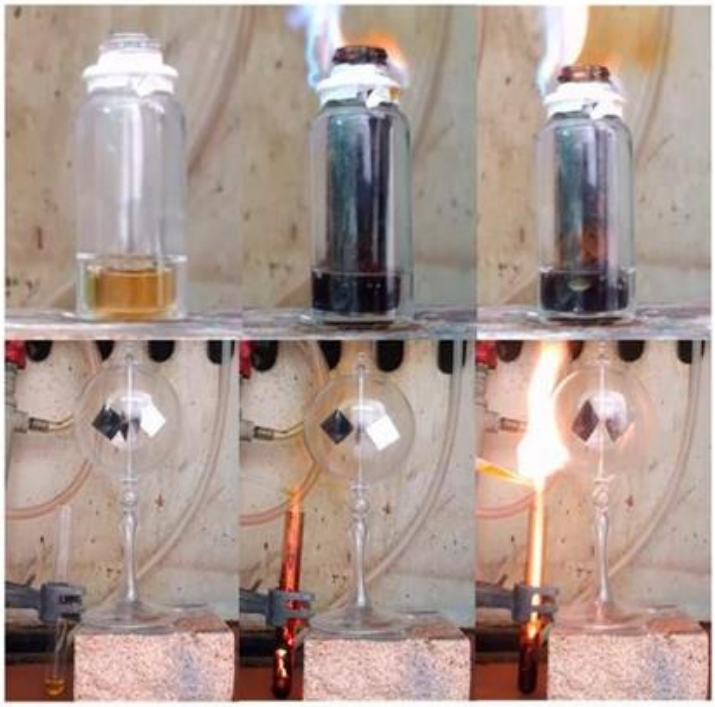

Figure 24: Top: a small glass vial filled with furfuryl alcohol was firmly fitted inside a bigger one containing acetone, as shown in the set up above. Acetone in the outer vial did not come into direct contact with the furfuryl alcohol in the inner vial. Teflon tape was placed at the contact of the fitted vials near the top rim in order to prevent flammable acetone vapor from escaping. The hypergolic reaction between furfuryl alcohol and fuming nitric acid HNO_3 released enough heat to boil acetone (boiling point 56 °C). The middle photo shows small bubbles that grew larger upon gradual heating of acetone to boiling (right photo). Bottom: a Crookes radiometer, initially at rest, was placed into motion by the released heat (*e.g.*, notice how the polished side of the depicted vane changed position upon rotation). Spinning was relatively slow due to non-uniform heating of the radiometer.

3.2. Sodium peroxide Na_2O_2

In this section we present the synthesis of carbon nanosheets and fullerols (or hydroxylated fullerenes) through spontaneous ignition of coffee-Na_2O_2 and C_{60}-Na_2O_2 hypergolic mixtures, respectively, with sodium peroxide Na_2O_2 acting as strong oxidizer (*e.g.*, source of highly concentrated H_2O_2) [8]. In the first case, a mixture of coffee grains and sodium peroxide Na_2O_2 was ignited with a small amount of water to result in a crude carbon residue that after it had been thoroughly washed afforded a fine black powder (Figure 25).

Figure 25: Left-to-right: coffee grains were mixed with sodium peroxide Na_2O_2 beads in a porcelain dish. Subsequent addition of water caused ignition of the mixture towards the formation of a crude carbon residue. After thorough washings, a fine black powder was obtained.

AFM study of the as-derived carbon showed the presence of large nanosheets with thickness 1.5-2.5 nm (Figure 26, top); the nanosheet morphology was additionally confirmed by TEM microscopy (Figure 26, bottom).

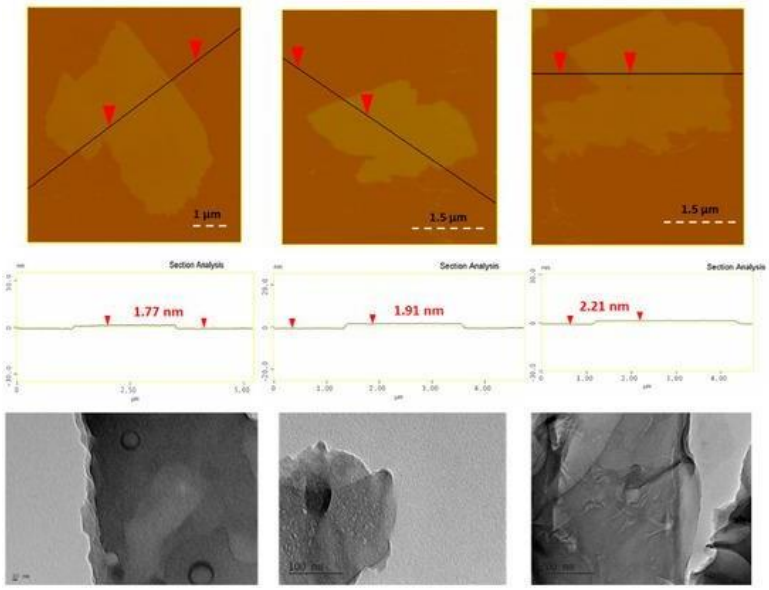

Figure 26: Top: AFM images of cross sectional analysis of selected carbon nanosheets. Bottom: representative TEM images of the sheets.

The coffee-derived nanosheets could be used as pigment in water glass paints for solar energy harvesting. Water glass refers to an aqueous solution of the inorganic polymer sodium silicate (40 %) that can wrap and electrostatically stabilize any dispersed solid. To this aim, carbon nanosheets were mechanically mixed with water glass to create the paint. The paint was then spread over a piece of paper with a brush and left to dry at room temperature (see the corresponding black square drawing in Figure 27, top). A similar drawing using analogous CuO paint was also sketched in a separate piece of paper (Figure 27, top); cupric oxide is a reference black pigment that is often used in solar water heaters [33]. Following, both coatings were illuminated under an infrared lamp at the same distance and for the same time (20 s) prior to scanning with a thermal camera. As it can be seen from Figure 27, bottom, carbon nanosheets and cupric oxide developed comparable temperatures (100-120 °C) under identical conditions. Hence, thanks to their flat surface and blackness, the nanosheets could be promising solar

energy absorbents [34].

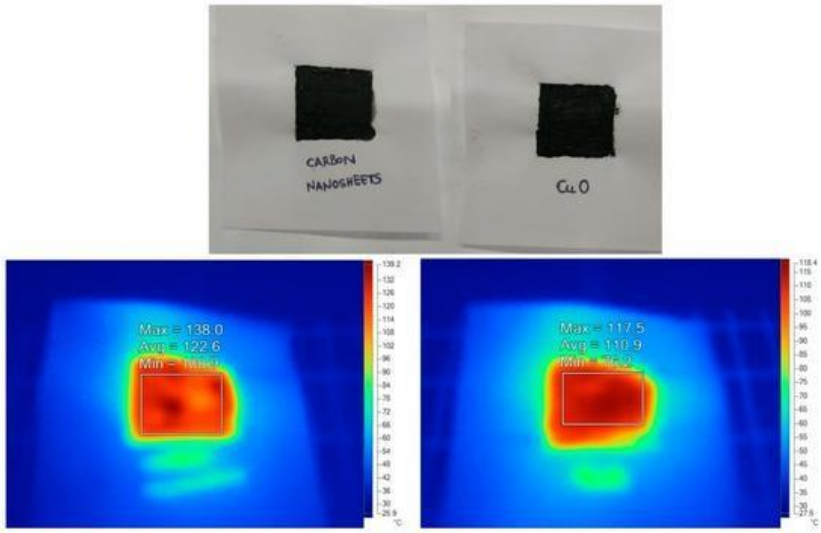

Figure 27: Top: dry carbon nanosheet and CuO paints on paper sheet (black squares). Bottom: the corresponding thermal camera images after 20 s illumination with infrared lamp (left: carbon nanosheets; right: CuO). Both samples developed comparable temperature after illumination under identical conditions, thus demonstrating that the coffee-derived carbon nanosheets were effective solar energy absorbents.

The heat and light produced from the spontaneous reaction of coffee with sodium peroxide Na_2O_2 was utilized in the generation of useful work. In one example, a miniature silicon photovoltaic panel connected with a green LED light was placed above the ignition mixture with the front side facing down the mixture at certain distance (Figure 28, top). Upon aqueous ignition, the produced thermal radiation and light turned on the LED light (Figure 28, top), thus acting as a sort of thermophotovoltaic [35]. In another example, the heat produced from the hypergolic mixture was exploited in the thermal decomposition of ferric acetate into magnetic iron oxide [36, 37]. For this purpose, a quartz tube charged with ferric acetate was dipped into an alumina crucible containing the hypergolic mixture (Figure 28, bottom). Aqueous ignition of the mixture provided the necessary heat for the thermal decomposition of the precursor inside the tube into magnetic iron oxide (Figure 28, bottom).

Figure 28: Top: ignition of the coffee-Na_2O_2 mixture by water generated enough thermal radiation and light to turn on a

miniature silicon photovoltaic device. Bottom: the water ignitable mixture served as a heat source for the in situ thermal transformation of ferric acetate (orange powder at far-left) into magnetic iron oxide (black solid at far-right). For this purpose, a small quartz tube was charged with the precursor and then dipped into the water ignitable mixture. Notice the release of smoke from the top rim of the tube due to thermal decomposition of ferric acetate.

The second case refers to the mechanochemical ignition of the C_{60}-Na_2O_2 pair towards the formation of hydroxylated fullerenes, namely fullerols [38] (Figure 29). To this aim, C_{60} powder was crushed in the presence of Na_2O_2 using a stainless steel mortar and pestle. Due to rapid oxidation of the carbon clusters by the peroxide, the mixture ignited spontaneously within few seconds. The product after it had been washed successively with concentrated HCl aqueous solution, water and acetone afforded a dark brown powder made up of fullerol clusters having the formula $C_{60}(OH)_7 \cdot 4H_2O$. The clusters were soluble in water after mild alkaline treatment with NaOH, the latter neutralizing the acidic phenolic protons into ionic phenolate groups that conferred aqueous solubility (Figure 29).

Figure 29: Crushing fullerenes in the presence of sodium peroxide Na_2O_2 beads in a stainless steel mortar and pestle caused ignition of the mixture as evidenced by the generation of bright flash. Washing of the product led to a dark brown powder, namely fullerols. Fullerols were soluble in water by mild alkaline treatment (far-right photo).

AFM study of the aqueous-soluble fraction revealed the presence of large globular nanoparticles with size in the range 15-25 nm (Figure 30). Fullerol typically has a size of 1.5 nm; however, it is well-known to form larger aggregates and eventually fullerol nanoparticles (10-60 nm) as a result of strong hydrogen bonding and π-π interactions between adjacent clusters [39].

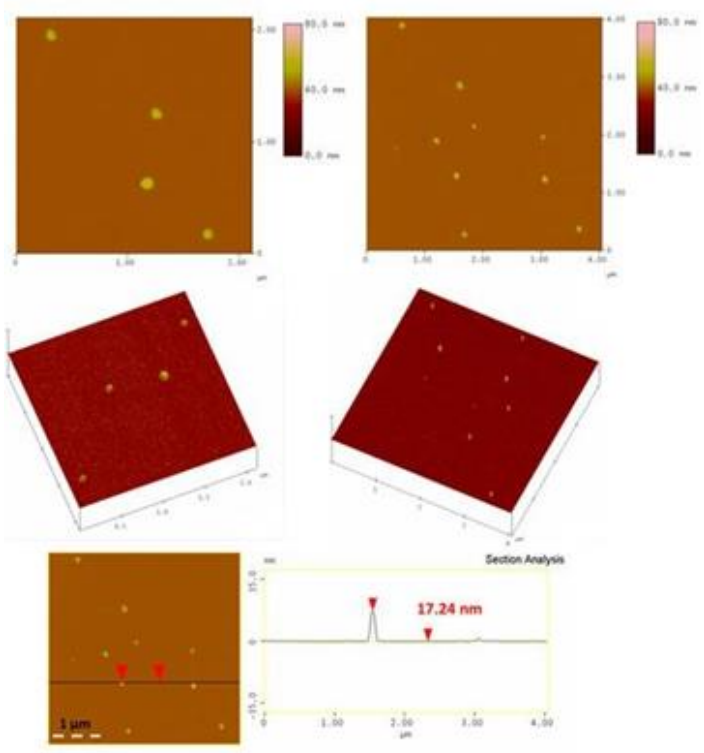

Figure 30: Representative AFM height images (top), 3D morphology (middle) and cross section analysis profile (bottom) of the globular fullerol nanoparticles.

3.3. Chlorine Cl_2

In this section we exploit a classic chemistry demonstration experiment based on the reaction of acetylene with chlorine towards the formation of highly crystalline graphite at ambient conditions (Figure 31) [6]. Acetylene and chlorine were generated in situ by the addition of calcium carbide (CaC_2) in concentrated HCl solution, followed by quick addition of domestic bleach (NaClO). The released gases reacted spontaneously upon contact, giving bursts of yellow flame, leaving highly crystalline graphite deposits in the aqueous phase. Taking into consideration that the preparation of synthetic graphite requires very high temperatures in order to achieve complete graphitization [40], the present method appeared as a quite appealing and milder alternative towards synthetic graphite.

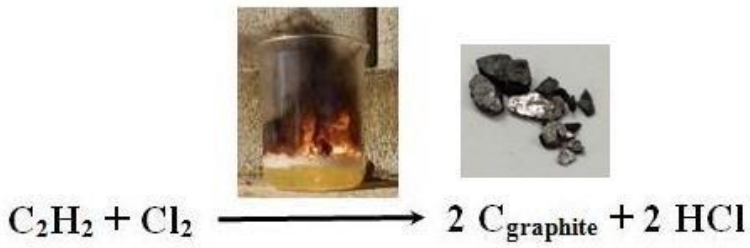

Figure 31: Synthesis of highly crystalline graphite from spontaneous ignition of in situ derived acetylene and chlorine at ambient conditions. The obtained conductive chunks had the lustrous grey appearance of graphite.

The XRD pattern (Figure 32, top) of the as-derived graphite showed a sharp diffraction peak attributed to the (002) reflection

of graphite, confirming a high degree of graphitization [41]. In addition, very weak reflections due to iron-based (α-Fe_2O_3, Fe, Fe_3C) and SiC impurities from the starting calcium carbide were also observed. On the other hand, the Raman spectrum (Figure 32, bottom) displayed two strong bands at 1582 cm^{-1} (G: sp^2 carbon) and 2713 cm^{-1} (2D), as well as weaker bands at 1348 cm^{-1} (D: sp^3 carbon), 2458 cm^{-1} (D + D"), 2945 cm^{-1} (D + G) and 3247 cm^{-1} (2D') [42]. The peak positions of the 2D and G bands, together with their intensity ratio, were well correlated with multilayer graphite. Furthermore, the intensity ratio I_D/I_G of the synthetic graphite was found at 0.15 (*i.e.*, in the range of 0.1-0.2 expected for highly crystalline graphite), whereas the full-width half-maximum (FWHM) of the sharp G band was 20 cm^{-1}, thus also indicating the formation of highly crystalline graphite. Most importantly, the XRD pattern and Raman spectrum of the present sample were very similar to those of commercial synthetic graphite presented elsewhere [6].

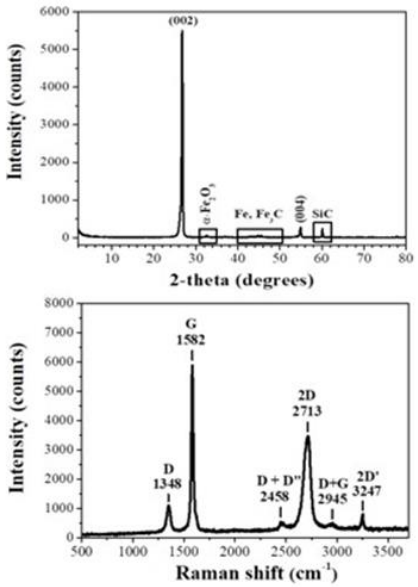

Figure 32: XRD pattern (top) and Raman spectrum (bottom) of the as-derived synthetic graphite.

AFM study (Figure 33, top) revealed the presence of graphite plates with thickness 15-20 nm and lateral size 2-5 μm (*e.g.*, thick micron-sized plates). The thickness of the plates exceeded the value of 5-10 nm for graphene nanosheets, hence pointing to multilayer graphite. In a practical use, we made a conductive ink by hand mixing a small amount of the prepared graphite powder with water glass (sodium silicate aqueous solution 40 %) as a binder. The ink was spread on a paper, leaving behind a flexible conductive trace after drying (Figure 33, top inset). In another example, we produced graphene using the liquid-phase exfoliation technique [21]. To this aim, the synthetic graphite was suspended by sonication in dimethylformamide and the suspension was left at rest for few days prior to collecting the supernatant as a clear colloid giving a strong Tyndall effect using a green laser pointer (Figure 33, bottom inset). According to AFM, the colloid contained micron-sized thin sheets with thickness 1-1.3 nm (Figure 33, bottom).

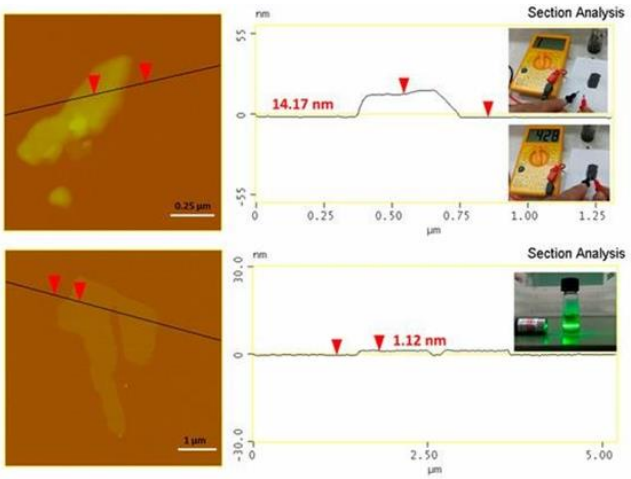

Figure 33: AFM images and height profiles of the synthetic graphite (top) and derived graphene (bottom). The top inset shows the waterborne conductive ink made of water glass and the synthetic graphite. The ink was applied on a piece of paper using a small paintbrush, leaving a flexible conductive trace after drying (note that paper itself is insulator). The bottom inset shows the colloidal dispersion of graphene in dimethylformamide exhibiting a strong Tyndall effect with a green laser pointer.

3.4. Bromine Br_2

In this section it is presented an interesting route to carbon from ferrocene without pyrolysis. Specifically, the direct contact of the metallocene with liquid bromine Br_2 at ambient conditions released rapidly and spontaneously carbon soot that after it had been thoroughly washed gave a fine black powder (Figure 34) [9]. Due to the strong exothermic character of the reaction (*e.g.*, sparks were occasionally observed upon contact of the reagents), the temperature was raised from room temperature to maximum 35-40 °C. It is likely that liquid bromine Br_2 acted as a coolant during reaction, removing most of the released heat by evaporation.

Figure 34: Addition of ferrocene to liquid bromine Br_2 rapidly led to an exothermic reaction that released carbon soot partly deposited on the walls of the test tube. After collecting and washing the carbon residue, a fine black powder was obtained.

Similarly, cobaltocene and nickelocene fine powders also reacted the same way against liquid bromine Br_2, thus demonstrating the general character of the method (Figure 35).

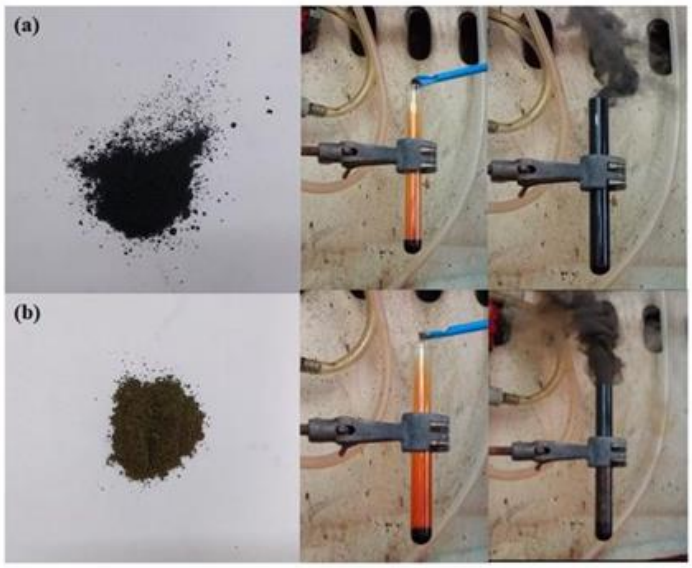

Figure 35: Cobaltocene (a) and nickelocene (b) fine powders reacted similarly to ferrocene against liquid bromine Br_2 to release carbon soot upon contact of the reagents.

TEM study of the ferrocene-derived carbon revealed the formation of carbon spheres (diameter 50-150 nm), nanosheets (submicron to micron lateral dimensions) and hollow spheres (outer diameter 50-150 nm; wall thickness 20-30 nm) (Figure 36). Dense and hollow spheres appeared to dominate the sample, followed by nanosheets to a less extent. Occasionally, some tubular hollow specimens were also observed.

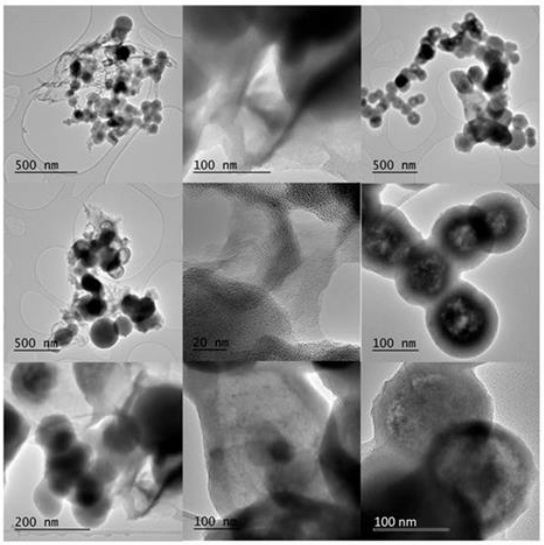

Figure 36: Representative TEM micrographs of carbon spheres (left column), nanosheets (middle column) and hollow spheres (right column).

Due to the presence of C-Br bonds on the carbon surface, the ferrocene-derived solid was modified through a nucleophilic substitution reaction with diglycolamine ($HOCH_2CH_2OCH_2CH_2NH_2$), thus conferring aqueous dispersability to the derivative (Figure 37, left). In addition, the derivative displayed bluish-green photoluminescence upon UV irradiation (Figure 37, left). This was also supported by the photoluminescence spectra of the dispersed solid, where maximum emission was observed in the bluish-green region of the visible spectrum (Figure 37, right). Such property was not displayed by the unmodified carbon solid or diglycolamine itself.

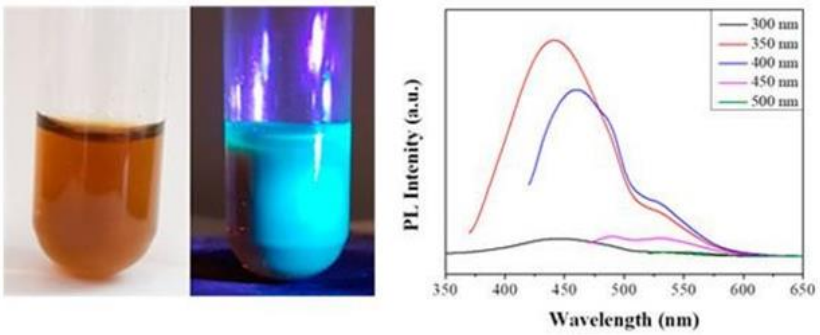

Figure 37: Left: aqueous dispersion of the diglycolamine-modified carbon under natural and UV light; Right: the corresponding photoluminescence spectra of the amine-modified carbon at different excitation wavelengths (λ_{ex} as inset).

From a mechanistic point of view, surface passivation is a fundamental photoluminescence-enhancing tool for improving emission from poor carbon emitters and usually involves amines as modifiers [43,44]. In addition, diglycolamine is frequently used as a linker in the synthesis of bioconjugate materials, thus making the fluorescent derivative appealing for bioimaging, cell labeling or drug delivery applications.

3.5. Self-ignition

In this section it is shown that pyrophoric lithium dialkylamides are versatile precursors towards the energy-friendly, fast, simple and effective synthesis of carbon nanosheets at ambient conditions [5]. Specifically, the nanosheets were produced by self-ignition in air of the pyrophoric salts lithium dimethylamide, lithium diethylamide and lithium diisopropylamide. For each case, a small amount of lithium dialkylamide was placed in a watch glass in open air for 10 min. In this way, a black solid was spontaneously formed due to self-ignition of the pyrophoric precursors in air. The crude residue after it had been thoroughly washed with an aqueous solution of HCl, water and acetone afforded a fine carbon powder (Figure 38).

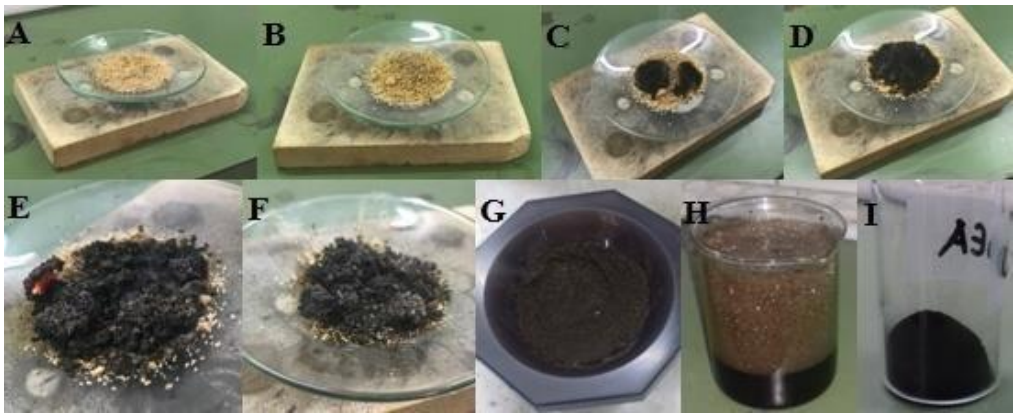

Figure 38: Photos A to D depict the gradual carbonization of the pyrophoric lithium diisopropylamide in air. Photo E shows a red-hot specimen due to self-ignition of the precursor in air. After carbonization and cooling at ambient temperature, the black residue shown in photo F was crashed into a fine powder (photo G) and added in acidified water (photo H). Treatment of the crude solid with acidified water released CO_2 gas due to the presence of Li_2CO_3 byproduct. Thorough washing and drying of the product with water and acetone gave a fine carbon powder (photo I).

Based on AFM and TEM analyses (Figure 39), the obtained powders from lithium dimethylamide, lithium diethylamide and lithium diisopropylamide predominantly contained carbon nanosheets with thicknesses between 2 and 3 nm and lateral dimensions in the submicron range.

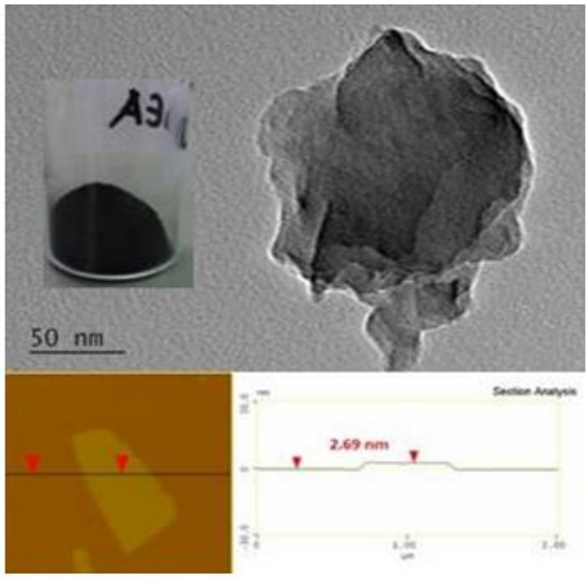

Figure 39: Individual carbon nanosheets obtained from self-ignition of lithium dialkylamides in air as shown under the TEM (top) and AFM (bottom) microscopes.

The carbonization process was spontaneous without the need of any external stimulus. As a matter of fact, the

heat released from the exothermic decomposition of the precursors could be further utilized to produce useful mechanical work through a Peltier thermoelectric device (Figure 40).

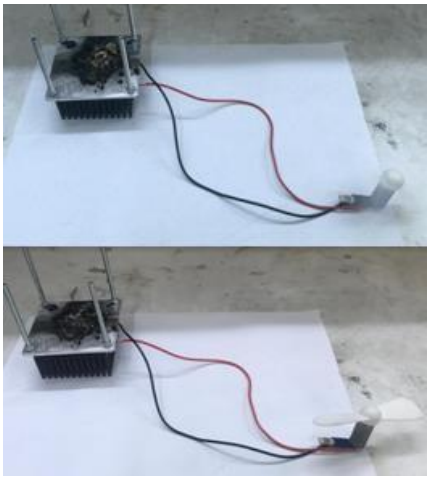

Figure 40: Top: the heat released from the self-ignition of lithium dimethylamide in air was used to rotate a small motor connected to a Peltier thermoelectric device. The device converted the temperature difference between the hot and cold sides of a sandwiched thermoelectric plate (Peltier) into electric voltage. The decomposing precursor on top provided the hot side while the heat sink at the bottom the cold side. Bottom: the rotor stopped after completion of the reaction and cooling of the products.

4. Hypergolic synthesis of inorganic materials

Although the majority of examples provided from our group pertained to carbon, hypergolic materials synthesis can be extended beyond carbon to include inorganic materials as well. For instance, in a previous work we have presented the rapid synthesis of inorganic materials (γ-Fe_2O_3, Cr_2O_3, Co, Ni, alloy CoNi) by the hypergolic ignition of certain metallocenes with fuming nitric acid HNO_3 [10]. In a follow up work, we have expanded the gallery of available inorganic nanostructures (TiO_2, ZrO_2, HfO_2 and MoO_2) by using closely related metallocene dichlorides and fuming nitric acid HNO_3 as starting reagents [14]. Therefore, metallocenes and metallocene dichlorides, thanks to their diverse structure and composition, appeared to be versatile reagents for the hypergolic synthesis of a wide range of inorganic materials with useful properties (magnetic, photocatalytic *etc.*). Below, hypergolic syntheses are given by the type of inorganic precursor used in combination with fuming nitric acid HNO_3 (metallocenes, metallocene dichlorides).

4.1. Metallocenes

Ferrocene and cobaltocene reacted hypergolicly with fuming nitric acid HNO_3 to afford magnetic nanopowders, such as γ-Fe_2O_3 and metallic Co, respectively [10]. Characteristically, the ignition of ferrocene by fuming nitric acid HNO_3 is illustrated in Figure 41. Both reactions completed within less than a minute, thus allowing rapid product formation at ambient conditions. The solids additionally contained residual carbon that however could be easily removed by mild heating of the powders in air.

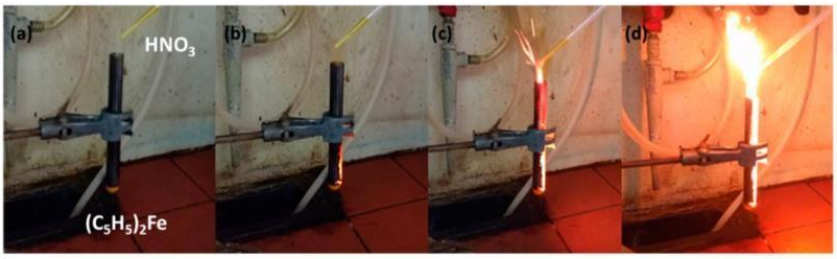

Figure 41: (a-d) Dropwise addition of fuming nitric acid HNO_3 into a test tube containing ferrocene powder resulted in the hypergolic ignition of the cyclopentadienyl compound by the acid and the subsequent formation of γ-Fe_2O_3 inside the tube. The magnetic solid was recovered by scratching off and washing the dark brown residue from inside the tube.

Figure 42 displays the indexed XRD patterns of the ferrocene-derived γ-Fe_2O_3 and cobaltocene-derived Co magnetic phases. In the former case, residual metallic Fe/Fe_3C phases were also detected. In the latter one, traces of cobalt oxides were additionally observed. Generally, ferrocene is well-known precursor to magnetic iron oxides [45,46]; similarly, cobaltocene is well-known precursor to metallic cobalt [47].

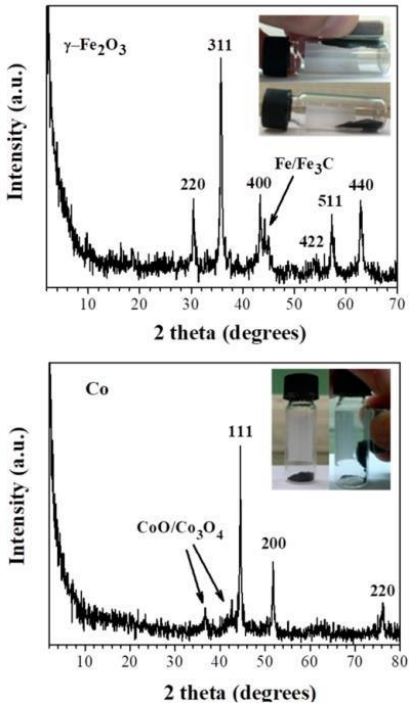

Figure 42: XRD patterns of the as-derived γ-Fe_2O_3 (top) and Co (bottom) magnetic solids. The insets show the strong attraction of the solids by Nd-magnet.

The AFM study of the magnetic solids revealed the presence of spherical nanoparticles with an average size of 8-11 nm for γ-Fe_2O_3 and 19-21 nm for metallic Co (Figure 43a,b). These values were in a good agreement with

those calculated from XRD and the Scherrer equation. The round shape of the nanoparticles was additionally confirmed by the corresponding 3D morphology images of the nanoparticles (Figure 43c,d).

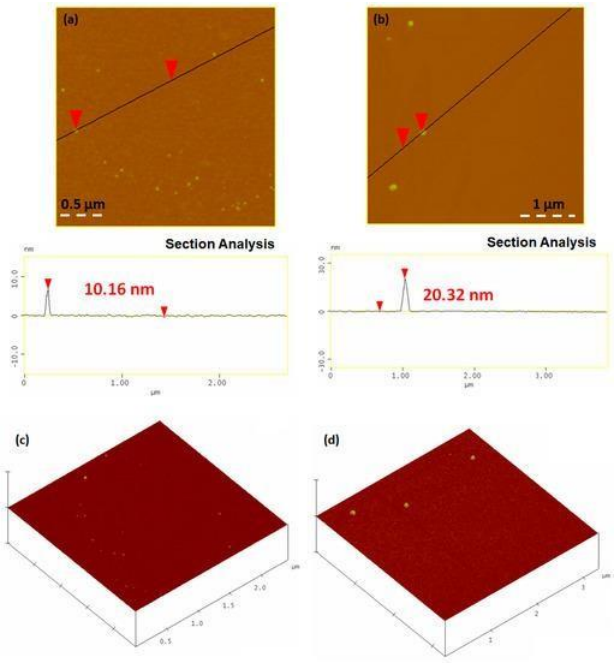

Figure 43: Cross-sectional analysis (a,b) and 3D morphology (c,d) of the magnetic nanoparticles. (a,c) γ-Fe_2O_3 and (b,d) Co.

The magnetic powders were strongly attracted by Nd-magnet as shown in the insets of Figure 42. In order to quantitatively determine the magnetic properties of the solids, the magnetization curves of the ferrocene- and cobaltocene-derived magnetic nanoparticles were recorded at room temperature (Figure 44). The nanoparticles did not exhibit hysteresis (*e.g.*, almost negligible coercivity). On the other hand, the saturation magnetization values were found to be 71 emu g^{-1} for γ-Fe_2O_3 and 70 emu g^{-1} for Co. These values were lower than those of the bulk phases (γ-Fe_2O_3: 83 emu g^{-1}; Co: 162 emu g^{-1}) due tothe quantum size effect, thus confirming the nanosized dimensions of the obtained particles.

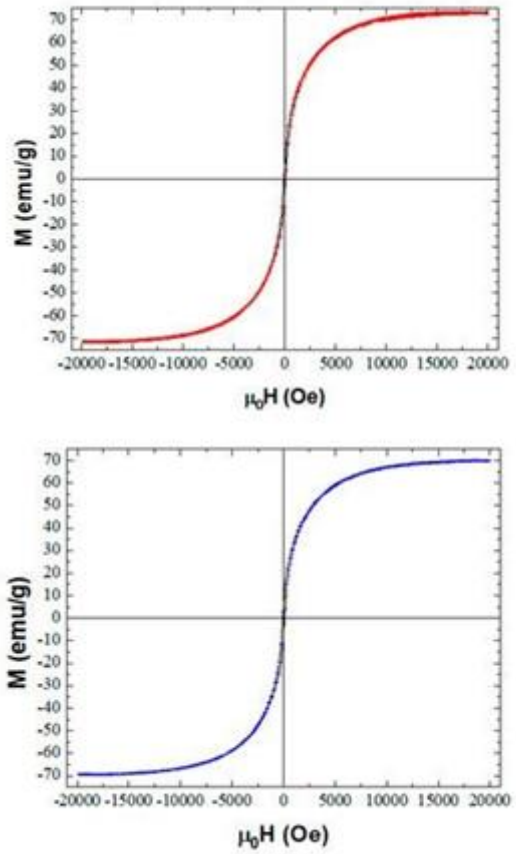

Figure 44: Magnetization curves of the ferrocene- (top red loop) and cobaltocene-derived (bottom blue loop) magnetic solids at room temperature.

Likewise cobaltocene, nickelocene afforded magnetic nickel nanoparticles after ignition with fuming nitric acid HNO_3. Moreover, the method was useful for the synthesis of alloy nanoparticles as well. For this purpose, equimolar amounts of cobaltocene and nickelocene were ground in the presence of acetone in a mortar and pestle to obtain a homogenous powder after drying. Acetone is a good solvent for both metallocenes, thus allowing molecular blending of the precursors. Following, the mixture was ignited by fuming nitric acid HNO_3 to afford CoNi magnetic nanoparticles displaying the characteristic (111), (200), and (220) reflections of the alloy [48]. Lastly, chromocene also reacted hypergolically with fuming nitric acid HNO_3 to give ceramic Cr_2O_3. The XRD patterns of all corresponding phases are given in Figure 45. Therefore, depending on the metallocene precursor many more inorganic materials can be foreseen and explored in this context.

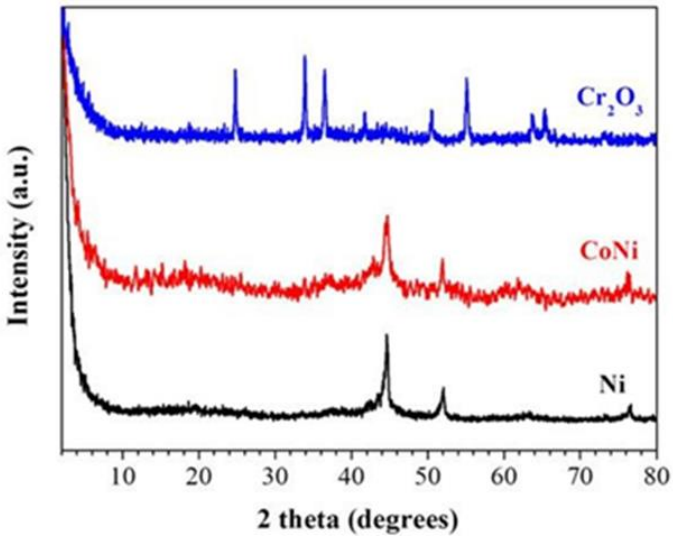

Figure 45: XRD patterns of the as-derived Ni (black line), CoNi alloy (red line) and Cr_2O_3 (blue line) phases.

4.2. Metallocene dichlorides

In the previous section metallocenes were shown to be versatile reagents in the hypergolic synthesis of inorganic materials, such as γ-Fe_2O_3, Cr_2O_3, Co, Ni and alloy CoNi. In this section, we go one step further by using metallocene dichlorides as precursors for the hypergolic synthesis of more inorganic phases, such as photocatalytic titania [14]. Metallocene dichlorides are closely related to metallocenes, thus expanding the arsenal of organometallic compounds that could be used in hypergolic materials synthesis. In particular, it is shown that hypergolic ignition of the titanocene dichloride-fuming nitric acid HNO_3 pair resulted in the fast and spontaneous formation of titania nanoparticles at ambient conditions (Figure 46). Because the sample additionally contained residual carbon, this was further heat treated at 500 °C in air in order to free the inorganic phase from residual carbon.

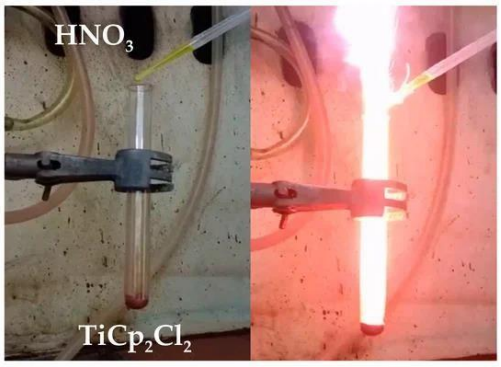

Figure 46: Dropwise addition of fuming nitric acid HNO_3 to titanocene dichloride in a test tube triggered spontaneous ignition towards titania formation.

The crystalline structure and phase composition of the calcined titania were studied by X-ray diffraction

(Figure 47). Accordingly, the calcined titania consisted of 70 % anatase and 30 % rutile phases based on Rietveld analysis. This anatase/rutile ratio was within the literature reported values for optimal TiO_2 photoreactivity [49-51].

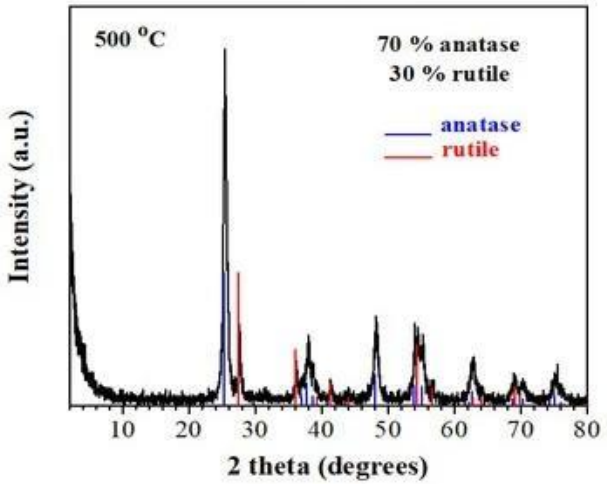

Figure 47: XRD pattern of the calcined titania showing the anatase and rutile phases at ratio 70/30.

The calcined titania was tested successfully in the removal of toxic hexavalent chromium [16,52] from water under UV irradiation. Ultraviolet light matches the energy band-gap of TiO_2, thus triggering electron transfer from the valence band to the conduction band of the solid [53,54]. The electrons sitting in the conduction band are then available to reduce the highly toxic Cr(VI) species into relatively harmless Cr(III) [53,54]. Thus, ultraviolet light is necessary in order to switch-on the photocatalytic activity of titania. The kinetics of Cr(VI) removal under UV irradiation at room temperature for calcined titania is depicted in Figure 48. Solutions of 50 mL containing 9 mg of sample and an initial Cr(VI) concentration of 5.5 mg/L at pH 3 (*e.g.*, acidic industrial wastewaters), were used to carry out the experiments. Accordingly, total Cr(VI) removal was achieved within 3 h under UV irradiation. As expected, the measurements without UV irradiation showed little capability for the removal of hexavalent chromium from the aqueous solution. Also noticeable was the fact that the combination of an acid environment and UV irradiation in the absence of titania led to an even less Cr(VI) removal of only 10 %, thus demonstrating the active role of TiO_2 in the photocatalytic process. For reasons of comparison, the efficiency of the commercial TiO_2 nanoparticles, AEROXIDE® TiO_2 P25 under identical conditions was also tested. In this case, the total Cr(VI) removal under UV irradiation was achieved within 2 h, thus being comparable to that of calcined titania.

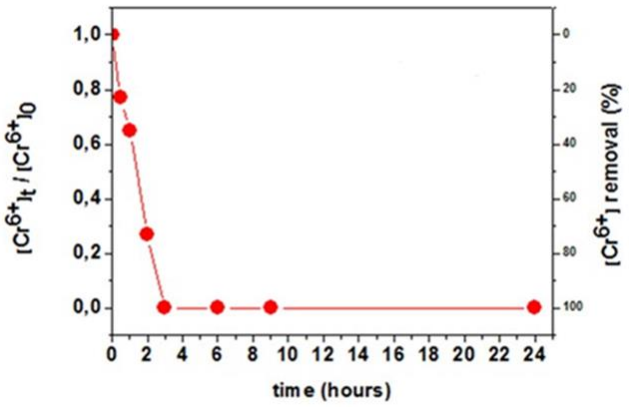

Figure 48: Effect of contact time on Cr(VI) removal from aqueous solution by the calcined titania under UV irradiation.

Likewise titanocene dichloride, the analogous zirconocene, hafnocene and molybdocene dichlorides also ignited rapidly and spontaneously upon contact with fuming nitric acid HNO_3 at ambient conditions (Figure 49) to give the corresponding ZrO_2, HfO_2 and MoO_2 phases with characteristic reflections in their XRD patterns (Figure 50). Similarly to the titania case, all the as-made samples also contained residual carbon that, however, could be easily removed by mild calcination in air. Therefore, metallocene dichlorides also appeared to be versatile organometallic reagents towards the hypergolic synthesis of diverse inorganic materials.

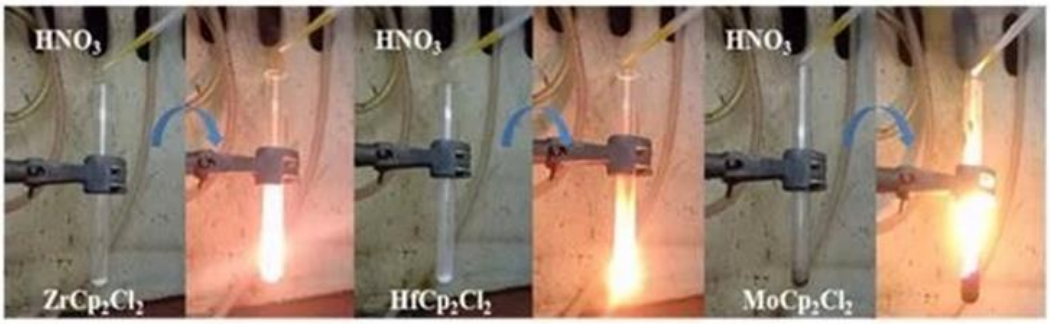

Figure 49: Hypergolic ignition of zirconocene, hafnocene and molybdocene dichlorides by fuming nitric acid HNO_3.

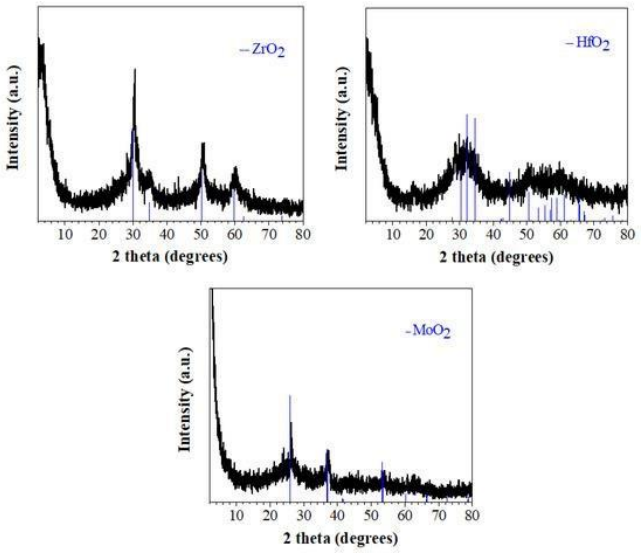

Figure 50: XRD patterns of the ZrO_2, HfO_2 and MoO_2 phases derived through hypergolic ignition of the corresponding metallocene dichlorides by fuming nitric acid HNO_3.

5. Large scale implementation

Hypergolic materials synthesis is safe to run on a small scale in the lab in spite of certain risks associated with hypergolic ignition or the use of hazardous reagents; however, for large-scale synthesis it would be necessary to build a pilot reactor that would borrow basic ideas from rocket fuel engineering. This is quite reasonable if one considers that lifting-off rockets in space also requires hypergolic fuel-oxidizer compositions similar to those employed in hypergolic materials synthesis. Hence, such a reactor could be possibly made up of an ignition chamber simultaneously connected to a fuel tank and an oxidizer tank, just like in chemical rocket engines [55] (Figure 51).

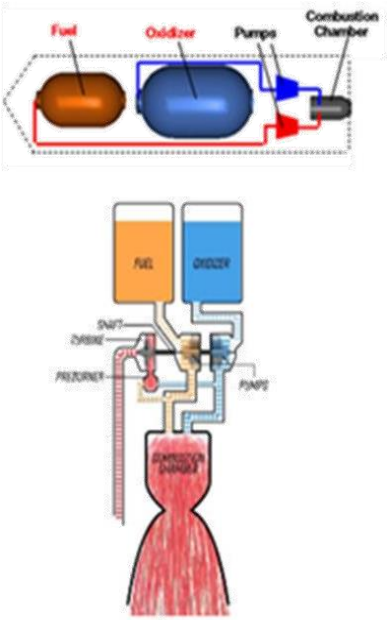

Figure 51: Chemical rocket engines (top) could form the technical basis behind the advancement of pilot reactors (bottom) towards large-scale hypergolic materials synthesis.

Although the method is still at its infancy, we believe that it has great potential to develop similarly to the flame spray pyrolysis technique in the near future. For instance, flame spray pyrolysis, which begun hesitantly decades ago due to serious hazards involved in the process (flammable methane, hot flames *etc.*), is now widely used in labs and industry thanks to a number of technical upgrades over time. Currently, several important materials (carbon black, fumed silica, P25 titania) are routinely produced *via* flame spray pyrolysis [56]. Another issue concerns the cost and toxicity of some of the reagents used in hypergolic materials synthesis, parameters that should be seriously taken into consideration in view of real investment and sustainability. For instance, some of the precursors used for synthesis (*e.g.*, conductive polymers, metallocenes, metallocene dichlorides) are considered expensive reagents, while some of the strong oxidizers employed (*e.g.*, fuming nitric acid HNO_3) are highly corrosive and hazardous. However, this seems to be an inevitable part of the method due to the prerequisite of hypergolicity, and certainly there are plenty more chemical options to be explored in the future in this direction. A last issue refers to the yields of hypergolic materials synthesis, which reasonably depended on the carbon or inorganic content of the corresponding precursors among others. The yields for carbon materials typically ranged between 2-25 %, whereas those for inorganic materials between 30-40 %. The latter yields are considered fair enough in inorganic synthesis; however, there is still space of improvement in the case of carbon. It is expected that control of certain reaction parameters, such as mixing rate of the fuel-oxidizer reagents and air-tight conditions, could substantially improve carbon yields.

6. Conclusions

Hypergolic materials synthesis is a radically new and versatile preparative technique in materials science that merits further attention towards research and development. The method is simple and easy in operation, fast and spontaneous at ambient conditions, allows the synthesis of carbon and inorganic functional materials, produces useful energy in the process, and may deal with rocket fuel waste disposal and valorization. Functional carbon materials of diverse morphologies, such as nanosheets, dots, hollow spheres, discs, fullerols and graphene/graphite, were obtained from hypergolic mixtures consisting of a combustible organic fuel and a strong oxidizer, such as fuming nitric acid HNO_3, sodium peroxide Na_2O_2, chlorine Cl_2, bromine Br_2 and self-ignition. On the other hand, functional inorganic materials, such as γ-Fe_2O_3, Cr_2O_3, Co, Ni, alloy CoNi, TiO_2, ZrO_2, HfO_2 and MoO_2, were obtained by the hypergolic ignition of diverse organometallic compounds, such as metallocenes and metallocene dichlorides, with fuming nitric acid HNO_3 as strong oxidizer. In all instances, the carbon or inorganic phase formation was fast, spontaneous and exothermic at ambient conditions, thus making hypergolic mixtures an interesting new source of functional nanomaterials. Although hypergolic material synthesis is safe to run on small scales, its large-scale and safe implementation in labs and industry would require technical upgrades and apparatuses analogous to those of chemical rocket engines. On top of that, the exploration of more chemical options towards the manufacture of an even larger variety of functional materials with interesting properties also remains a challenge. Overall, the present review aimed to show the wider applicability and generic character of hypergolic reactions in nanomaterials synthesis, namely hypergolic materials synthesis. It is believed that the new preparative technique has great potential to grow similarly to the

flame spray pyrolysis method, the latter based on ignition of flammable hydrocarbons inside suitably designed reactors for labs or industry.

Conflict of interest

The authors declared that they have no conflicts of interest to this work.

Acknowledgments

This study was funded by the project "National Infrastructure in Nanotechnology, Advanced Materials and Micro-/Nanoelectronics" (MIS-5002772) which was implemented under the action "Reinforcement of the Research and Innovation Infrastructure", funded by the Operational Programme "Competitiveness, Entrepreneurship and Innovation" (NSRF 2014-2020), and co-financed by Greece and the European Union (European Regional Development Fund).

References

1. Tavakoli A, Sohrabi M, Kargari A. A review of methods for synthesis of nanostructured metals with emphasis on iron compounds. Chem Pap 61 (2007): 151-170.
2. Sutka A, Mezinskis G. Sol-gel auto-combustion synthesis of spinel-type ferrite nanomaterials. Front Mater Sci 6 (2012): 128-141.
3. Ayuk E, Mariagoretti U, Samuel A. A review on synthetic methods of nanostructured materials. Chem Res J 2 (2017): 97-123.
4. Ganachari SV, Banapurmath NR, Salimath B, et al. Synthesis techniques for preparation of nanomaterials. In Handbook of Ecomaterials; Martínez LMT, Kharissova OV, Kharisov BI, Eds; Springer International Publishing: Cham, Switzerland, 2017: 1-21.
5. Baikousi M, Chalmpes N, Spyrou K, et al. Direct production of carbon nanosheets by self-ignition of pyrophoric lithium dialkylamides in air. Mater Lett 254 (2019): 58-61.
6. Chalmpes N, Spyrou K, Bourlinos AB, et al. Synthesis of highly crystalline graphite from spontaneous ignition of in situ derived acetylene and chlorine at ambient conditions. Molecules 25 (2020): 297.
7. Chalmpes N, Asimakopoulos G, Spyrou K, et al. Functional carbon materials derived through hypergolic reactions at ambient conditions. Nanomaterials 10 (2020): 566.
8. Chalmpes N, Spyrou K, Vasilopoulos KC, et al. Hypergolics in carbon nanomaterials synthesis: new paradigms and perspectives. Molecules 25 (2020): 2207.
9. Chalmpes N, Tantis I, Bakandritsos A, et al. Rapid carbon formation from spontaneous reaction of ferrocene and liquid bromine at ambient conditions. Nanomaterials 10 (2020): 1564.
10. Chalmpes N, Bourlinos AB, Šedajová V, et al. Hypergolic materials synthesis through reaction of fuming nitric acid with certain cyclopentadienyl compounds. C 6 (2020): 61.
11. Chalmpes N, Bourlinos AB, Talande S, et al. Nanocarbon from rocket fuel waste: the case of furfuryl alcohol-fuming nitric acid hypergolic pair. Nanomaterials 11 (2021): 1.
12. Chalmpes N, Moschovas D, Tantis I, et al. Carbon nanostructures derived through hypergolic reaction of conductive polymers with fuming nitric acid at ambient conditions. Molecules 26 (2021): 1595.
13. Chalmpes N, Moschovas D, Bourlinos AB, et al. Hypergolic ignition of 1,3-cyclodienes by fuming nitric

acid toward the fast and spontaneous formation of carbon nanosheets at ambient conditions. Micro 1 (2021): 15-27.

14. Chalmpes N, Asimakopoulos G, Baikousi M, et al. Hypergolic synthesis of inorganic materials by the reaction of metallocene dichlorides with fuming nitric acid at ambient conditions: the case of photocatalytic titania. Sci 3 (2021): 46.
15. Bourlinos AB. A new generation of carbon-containing hypergolic fuels based on water-ignitable C-NaH mixtures. J Nanotechnol Res 4 (2022): 1-9.
16. Casadevall M, da Cruz Fresco P, Kortenkamp A. Chromium(VI)-mediated DNA damage: oxidative pathways resulting in the formation of DNA breaks and abasic sites. Chem Biol Interact 123 (1999): 117-132.
17. Thomas A, Fischer A, Goettmann F, et al. Graphitic carbon nitride materials: variation of structure and morphology and their use as metal-free catalysts. J Mater Chem 18 (2008): 4893-4908.
18. Baker SN, Baker GA. Luminescent carbon nanodots: emergent nanolights. Angew Chem Int Ed 49(2010): 6726-6744.
19. Bourlinos AB, Zbořil R, Petr J, et al. Luminescent surface quaternized carbon dots. Chem Mater 24(2012): 6-8.
20. Essner JB, Kist JA, Polo-Parada L, et al. Artifacts and errors associated with the ubiquitous presence of fluorescent impurities in carbon nanodots. Chem Mater 30 (2018): 1878-1887.
21. Bourlinos AB, Georgakilas V, Zboril R, et al. Liquid-phase exfoliation of graphite towards solubilized graphenes. Small 5 (2009): 1841-1845.
22. Dimos K. Tuning carbon dots' optoelectronic properties with polymers. Polymers 10 (2018): 1312.
23. Zapsas G, Moschovas D, Ntetsikas K, et al. Segregation of maghemite nanoparticles within symmetric diblock copolymer and triblock terpolymer patterns under solvent vapor annealing. Materials 13 (2020): 1286.
24. Mariscal R, Maireles-Torres P, Ojeda M, et al. Furfural: a renewable and versatile platform molecule for the synthesis of chemicals and fuels. Energy Environ Sci 9 (2016): 1144-1189.
25. Iroegbu AO, Hlangothi SP. Furfuryl alcohol a versatile, eco-sustainable compound in perspective. Chem Afr 2 (2019): 223-239.
26. Munjal NL. Ignition catalysts for furfuryl alcohol-red fuming nitric acid bipropellant. AIAA J 8 (1970): 980-981.
27. Kulkarni SG, Bagalkote VS, Patil SS, et al. Theoretical evaluation and experimental validation of performance parameters of new hypergolic liquid fuel blends with red fuming nitric acid as oxidizer. Propellants Explos Pyrotech 34 (2009): 520-525.
28. Kulkarni S, Bagalkote V. Studies on pre-ignition reactions of hydrocarbon-based rocket fuels hypergolic with red fuming nitric acid as oxidizer. J Energet Mater 28 (2010): 173-188.
29. Bhosale MVK, Kulkarni SG, Kulkarni PS. Ionic liquid and biofuel blend: a low-cost and high performance hypergolic fuel for propulsion application. ChemistrySelect 1 (2016): 1921-1925.
30. Choura M, Belgacem NM, Gandini A. Acid-catalyzed polycondensation of furfuryl alcohol: mechanisms of chromophore formation and cross-linking. Macromolecules 29 (1996): 3839-3850.
31. Guigo N, Mija A, Zavaglia R, et al. New insights on the thermal degradation pathways of neat poly(furfuryl

alcohol) and poly(furfuryl alcohol)/SiO_2 hybrid materials. Polym Degrad Stab 94 (2009): 908-913.

32. Ahmad EEM, Luyt AS, Djoković V. Thermal and dynamic mechanical properties of bio-based poly(furfuryl alcohol)/sisal whiskers nanocomposites. Polym Bull 70 (2013): 1265-1276.
33. Karthick Kumar S; Suresh S, Murugesan S, et al. CuO thin films made of nanofibers for solar selective absorber applications. Sol Energy 94 (2013): 299-304.
34. Jönsson G, Fredriksson H, Sellappan R, et al. Nanostructures for enhanced light absorption in solar energy devices. Int J Photoenergy 2011 (2011): 939807.
35. Coutts TJ. A review of progress in thermophotovoltaic generation of electricity. Renew Sustain Energy Rev 3 (1999): 77-184.
36. Jewur SS, Kuriacose JC. Studies on the thermal decomposition of ferric acetate. Thermochim Acta 19 (1977): 195-200.
37. Pinheiro EA, Pereira de Abreu Filho P, Galembeck F, et al. Magnetite crystal formation from iron(III) hydride acetate. an ESR study. Langmuir 3 (1987): 445-448.
38. Vileno B, Marcoux PR, Lekka M, et al. Spectroscopic and photophysical properties of a highly derivatized C60 fullerol. Adv Funct Mater 16 (2006): 120-128.
39. Djordjevic A, Srdjenovic B, Seke M, et al. Review of synthesis and antioxidant potential of fullerenol nanoparticles. J Nanomater 2015 (2015): 567073.
40. Ramachandran VS, Beaudoin JJ. Handbook of carbon, graphite, diamond, and fullerenes: properties, processing, and applications; Elsevier Science & Technology Books: Norwich, NY, USA (2000).
41. Li ZQ, Lu CJ, Xia ZP, et al. X-ray diffraction patterns of graphite and turbostratic carbon. Carbon 45 (2007): 1686-1695.
42. Ramya AV, Manoj B, Mohan AN. Extraction and characterization of wrinkled graphene nanolayers from commercial graphite. Asian J Chem 28 (2016): 1031-1034.
43. Li L, Dong T. Photoluminescence tuning in carbon dots: surface passivation or/and functionalization, heteroatom doping. J Mater Chem C 6 (2018): 7944-7970.
44. Potsi G, Bourlinos AB, Mouselimis V, et al. Intrinsic photoluminescence of amine-functionalized graphene derivatives for bioimaging applications. Appl Mater Today 17 (2019): 112-122.
45. Amara D, Margel S. Solventless thermal decomposition of ferrocene as a new approach for the synthesis of porous superparamagnetic and ferromagnetic composite microspheres of narrow size distribution. J Mater Chem 21 (2011): 15764-15772.
46. Amara D, Margel S. Synthesis and characterization of elemental iron and iron oxidenano/microcomposite particles by thermal decomposition of ferrocene. Nanotechnol Rev 2 (2013): 333.
47. Dormans GJM, Meekes GJBM, Staring EGJ. OMCVD of cobalt and cobalt silicide. J Cryst Growth 114 (1991): 364-372.
48. Wei X-W, Zhou X-M, Wu K-L, et al. 3-D flower-like NiCo alloy nano/microstructures grown by a surfactant-assisted solvothermal process. CrystEngComm 13 (2011): 1328-1332.
49. Ohno T, Sarukawa K, Tokieda K, et al. Morphology of a TiO_2 photocatalyst (Degussa, P-25) consisting of anatase and rutile crystalline phases. J Catal 203 (2001): 82-86.

50. Su R, Bechstein R, Sø L, et al. How the anatase-to-rutile ratio influences the photoreactivity of TiO_2. J Phys Chem C 115 (2011): 24287-24292.
51. He J, Du Y-E, Bai Y, et al. Facile formation of anatase/rutile TiO_2 nanocomposites with enhanced photocatalytic activity. Molecules 24 (2019): 2996.
52. Pakade VE, Tavengwa NT, Madikizela LM. Recent advances in hexavalent chromium removal from aqueous solutions by adsorptive methods. RSC Adv 9 (2019): 26142-26164.
53. Shaban Y. Effective photocatalytic reduction of Cr(VI) by carbon modified (CM)-n-TiO_2 nanoparticles under solar irradiation. World J Nano Sci Eng 3 (2013): 154-160.
54. Ali MEM, Assirey EA, Abdel-Moniem SM, et al. Low temperature-calcined TiO_2 for visible light assisted decontamination of 4-nitrophenol and hexavalent chromium from wastewater. Sci Rep 9 (2019): 19354.
55. El-Sayed A. Fundamentals of aircraft and rocket propulsion (Chapter 11th). In Fundamentals of aircraft and rocket propulsion; Springer: London, UK, 2016.
56. Pratsinis SE. Flame aerosol synthesis of ceramic powders. Prog Energy Combust Sci 24 (1998): 197-219.